

**Argonne National Laboratory**

**COMPARISON OF THE VARIOUS  
NEUTRONIC REPRESENTATIONS  
FOR EBR-II ANALYSES**

by

**J. T. Madell and R. E. Jarka**

The facilities of Argonne National Laboratory are owned by the United States Government. Under the terms of a contract (W-31-109-Eng-38) between the U. S. Atomic Energy Commission, Argonne Universities Association and The University of Chicago, the University employs the staff and operates the Laboratory in accordance with policies and programs formulated, approved and reviewed by the Association.

#### MEMBERS OF ARGONNE UNIVERSITIES ASSOCIATION

The University of Arizona	Kansas State University	The Ohio State University
Carnegie-Mellon University	The University of Kansas	Ohio University
Case Western Reserve University	Loyola University	The Pennsylvania State University
The University of Chicago	Marquette University	Purdue University
University of Cincinnati	Michigan State University	Saint Louis University
Illinois Institute of Technology	The University of Michigan	Southern Illinois University
University of Illinois	University of Minnesota	University of Texas
Indiana University	University of Missouri	Washington University
Iowa State University	Northwestern University	Wayne State University
The University of Iowa	University of Notre Dame	The University of Wisconsin

#### LEGAL NOTICE

This report was prepared as an account of Government sponsored work. Neither the United States, nor the Commission, nor any person acting on behalf of the Commission:

A. Makes any warranty or representation, expressed or implied, with respect to the accuracy, completeness, or usefulness of the information contained in this report, or that the use of any information, apparatus, method, or process disclosed in this report may not infringe privately owned rights; or

B. Assumes any liabilities with respect to the use of, or for damages resulting from the use of any information, apparatus, method, or process disclosed in this report.

As used in the above, "person acting on behalf of the Commission" includes any employee or contractor of the Commission, or employee of such contractor, to the extent that such employee or contractor of the Commission, or employee of such contractor prepares, disseminates, or provides access to, any information pursuant to his employment or contract with the Commission, or his employment with such contractor.

Printed in the United States of America  
Available from

Clearinghouse for Federal Scientific and Technical Information  
National Bureau of Standards, U. S. Department of Commerce  
Springfield, Virginia 22151

Price: Printed Copy \$3.00; Microfiche \$0.65

ARGONNE NATIONAL LABORATORY  
9700 South Cass Avenue  
Argonne, Illinois 60439

COMPARISON OF THE VARIOUS  
NEUTRONIC REPRESENTATIONS  
FOR EBR-II ANALYSES

by

J. T. Madell\* and R. E. Jarka

EBR-II Project

February 1970

---

\*Now with Applied Physics Division.





## TABLE OF CONTENTS

	<u>Page</u>
NOMENCLATURE . . . . .	10
ABSTRACT . . . . .	11
I. INTRODUCTION. . . . .	11
II. REPRESENTATION OF THE PHYSICAL SYSTEM FOR NEUTRONIC CALCULATIONS . . . . .	12
A. Introduction . . . . .	12
B. Types of Subassemblies . . . . .	13
C. Radial Representation of EBR-II . . . . .	16
D. Preparation of Input Specifications . . . . .	18
III. NEUTRON CROSS-SECTION SETS. . . . .	21
A. Development of Sets 236, 23606, 23605, 238, 23806, and JM31F . . . . .	21
1. Set 236 . . . . .	21
2. Set 23606. . . . .	22
3. Set 23605. . . . .	25
4. Set 238 . . . . .	25
5. Set 23806. . . . .	28
6. Set JM31F . . . . .	28
B. Comparison of the Neutron Cross-section Sets . . . . .	30
C. Analysis of the Weighting Spectrum . . . . .	32
IV. INVESTIGATION OF ONE-DIMENSIONAL REPRESENTATION OF EBR-II . . . . .	34
A. Comparison of Results from Diffusion and Transport Calculations . . . . .	34
B. Effect of Geometrical Approximations. . . . .	36
1. Calculations Using a Cylindrical Representation. . . . .	36
2. Calculations Using a Spherical Representation. . . . .	39

## TABLE OF CONTENTS

	<u>Page</u>
V. INVESTIGATION OF TWO-DIMENSIONAL REPRESENTATION OF EBR-II. . . . .	41
A. Introduction. . . . .	41
B. Comparison of Eigenvalues of the Eight Two-dimensional Calculations . . . . .	43
C. Comparison of Fluxes at the Core Center. . . . .	43
D. Comparison of Fission Ratios. . . . .	44
E. Comparison of Neutron Spectra. . . . .	44
1. Comparison of the 22-group Spectra . . . . .	44
2. Comparison of the Six-group Spectra. . . . .	46
F. Nonseparability of the Radial and Axial Fluxes . . . . .	48
G. High-energy Reactions in EBR-II . . . . .	51
H. Comparison of the Distribution of Power by Region . . . . .	53
I. Comparison of Fission-density Values . . . . .	54
J. Comparison of $^{235}\text{U}$ Fission Rate. . . . .	56
K. Comparison of Results from One- and Two-dimensional Calculations . . . . .	58
REFERENCES. . . . .	61

## LIST OF FIGURES

<u>No.</u>	<u>Title</u>	<u>Page</u>
1.	Horizontal Section of EBR-II . . . . .	13
2.	Regional and Dimensional Description of Various Types of Subassemblies for EBR-II . . . . .	14
3.	Hexagonal Rows of EBR-II Subassemblies with Annular Region for Fifth Row. . . . .	16
4.	Fission Densities for 6- and 15-region Representations of EBR-II Core . . . . .	17
5.	Normalized Distribution of $\sigma_f^{25}$ Reaction Rate for 6- and 15-region Representations of EBR-II Core . . . . .	17
6.	Normalized Distribution of $\sigma_c^{25}$ Reaction Rate for 6- and 15-region Representations of EBR-II Core . . . . .	17
7.	Normalized Distribution of $\sigma_f^{28}$ Reaction Rate for 6- and 15-region Representations of EBR-II Core . . . . .	18
8.	Normalized Distribution of $\sigma_f^{28}$ to $\sigma_f^{25}$ Reaction Ratio for 6- and 15-region Representations of EBR-II Core . . . . .	18
9.	Comparison of Real- and Adjoint-flux Spectra from Sets 236 and 23606 . . . . .	24
10.	Comparison of Real- and Adjoint-flux Spectra from Sets 236 and 23605 . . . . .	26
11.	Fission-density Distribution from $S_2$ Transport and Diffusion Calculations . . . . .	35
12.	Pictorial Representation of Two Approaches to Calculating Criticality in One-dimensional Cylindrical Geometry . . . . .	36
13.	Representation of EBR-II for Two-dimensional (r,z) Calculations with Region Numbers and Identification. . . . .	42
14.	Flux Spectra of Set 238 at Five Locations in Run 31F, Obtained from DIF-2D Calculations . . . . .	45
15.	Flux Spectra of Set 238 at Five Locations in Run 31F, Obtained from DOT Calculations ( $S_2$ ) . . . . .	45
16.	Normalized Axial Flux Distribution by Group at 28.4-cm Radius for Run 27A. . . . .	49
17.	Normalized Axial Flux Distribution by Group at 36.5-cm Radius for Run 27A. . . . .	49

## LIST OF FIGURES

<u>No.</u>	<u>Title</u>	<u>Page</u>
18.	Normalized Axial Flux Distribution by Group at 50.0-cm Radius for Run 27A. . . . .	49
19.	Normalized Axial Flux Distribution by Group at 28.4-cm Radius for Run 31F. . . . .	50
20.	Normalized Axial Flux Distribution by Group at 36.5-cm Radius for Run 31F. . . . .	50
21.	Normalized Axial Flux Distribution by Group at 50.0-cm Radius for Run 31F. . . . .	50
22.	Flux Spectrum above 1.35 MeV at Core Center in Run 31F. . . .	52
23.	Flux Spectrum above 1.35 MeV at Interface between Core and Radial Blanket in Run 31F. . . . .	52
24.	Flux Spectrum above 1.35 MeV at Interface between Core and Upper Axial Reflector in Run 31F. . . . .	52
25.	Flux Spectrum above 1.35 MeV at ~15 cm above Core in Run 31F. . . . .	52
26.	Flux Spectrum above 1.35 MeV at ~15 cm into Radial Blanket in Run 31F. . . . .	52

## LIST OF TABLES

<u>No.</u>	<u>Title</u>	<u>Page</u>
I.	Material Volume Fractions in the 14 Types of Subassemblies for EBR-II . . . . .	15
II.	Atomic Densities of Depleted Uranium, Steel, and Fissium at 700°F . . . . .	19
III.	Partial Computer Listing of Loading Data for Run 26 . . . . .	19
IV.	Description of Cross-section Set 236 . . . . .	22
V.	Description of Cross-section Sets 23606 and 23605 . . . . .	23
VI.	Reactivity Worths of Various Materials due to a 1% Decrease in Density as Calculated by Cross-section Sets 236, 23606, and 23605 . . . . .	24
VII.	Atomic Densities of Nuclides Used in Generating Weighting Spectra of Set 238 . . . . .	27
VIII.	Description of Cross-section Sets 238 and 23806 . . . . .	27
IX.	Group Structure of Cross-section Set JM31F . . . . .	28
X.	Atomic Densities of Nuclides Used in Generating the Weighting Spectra of Set JM31F . . . . .	29
XI.	Description of Cross-section Set JM31F . . . . .	29
XII.	Composition of Simplified (Three-region, Spherical Geometry) Model of EBR-II . . . . .	30
XIII.	Values of $k_{eff}$ of Spherical Representation of EBR-II for Various Cross-section Sets, Weighting Spectra, and Neutronic Models . . . . .	31
XIV.	Component and Total Values of $\Delta k/k$ for the Exchange of Reflector- and Blanket-weighted Cross Sections in the Reflector Region . . . . .	32
XV.	Flux at Core Center and Edge from Diffusion and $S_2$ and $S_4$ Transport Calculations . . . . .	34
XVI.	Fraction of Flux at Core Center and Edge per Group from Diffusion Calculations and $S_2$ and $S_4$ Transport Calculations . . . . .	35
XVII.	Results from the Eight Cases Using One-dimensional, Cylindrical Representations of EBR-II at 50 MWt . . . . .	37
XVIII.	Fission Densities at 50 MWt by Row from One-dimensional, Cylindrical Calculations of Runs 27A and 31F . . . . .	38

## LIST OF TABLES

<u>No.</u>	<u>Title</u>	<u>Page</u>
XIX.	Fraction of Power by Region from One-dimensional, Cylindrical Calculations of Runs 27A and 31F . . . . .	39
XX.	Results from the Four Cases Using One-dimensional, Spherical Representation of EBR-II at 50 MWt. . . . .	40
XXI.	Description and Partial Results of the Two-dimensional Calculations of EBR-II, Run 31F at 50 MWt. . . . .	42
XXII.	Fraction of Flux per Group at Five Locations for the Eight Two-dimensional Calculations of Run 31F. . . . .	47
XXIII.	Rate of Various High-energy Reactions per Gram of Target Nuclide at Three Locations in EBR-II, Run 31F. . . . .	53
XXIV.	Fraction of Power by Region from Two-dimensional Diffusion and Transport Calculations for Run 31F . . . . .	54
XXV.	Radial Fission Densities from Two-dimensional Transport Calculations for Runs 27A and 31F along Core Midplane at 50 MWt. . . . .	55
XXVI.	Axial Fission Densities from Two-dimensional Transport ( $S_4$ ) Calculations for Run 31F at Four Radial Positions at 50 MWt. . . . .	55
XXVII.	Normalized Radial $^{235}\text{U}$ Fission Rates along Core Midplane from Diffusion and Transport Calculations of Run 31F . . . . .	57
XXVIII.	Normalized Axial $^{235}\text{U}$ Fission Rates along Core Centerline from Diffusion and Transport Calculations of Run 31F . . . . .	58
XXIX.	Values of the Flux at the Core Center Obtained from One-dimensional Cylindrical Calculations for Run 31F at 50 MWt. . . . .	59
XXX.	Fraction of Core Center Flux from One- and Two-dimensional Cylindrical Calculations in the First 14 Groups of Set 238 for Run 31F . . . . .	60



# NOMENCLATURE

$A_0$  = Avogadro's number

$(AW)_i$  = Atomic weight of the  $i$ th heavy isotope

BU = Heavy atomic percent burnup

$H_C$  = Core height, cm

$H_E$  = Equivalent bare core height, cm

$j$  = Energy group

$N$  = Total number of subassemblies enclosed within radius  $r$

$r$  = Radial dimension of a region, cm

$r_0$  = Radius of the center subassembly, cm

$V$  = Volume of a subassembly core region

$W_i^n$  = Weight of the  $i$ th heavy isotope in the  $n$ th subassembly of the  $R$ th region, g

$z$  = Distance from core midplane, cm

$\rho_{FPP}$  = Atomic density of the fission-product pair, atoms/cm<sup>3</sup>

$\rho_i^R$  = Atomic density of the  $i$ th heavy isotope in the  $R$ th region, atoms/cm<sup>3</sup>

$\rho_{i0}$  = Initial density of  $i$ th heavy isotope

$\Sigma_{trj}$  = Macroscopic transport cross section for the  $j$ th energy group

$\varphi_0$  = Flux at midplane, n/cm<sup>2</sup>/sec

$\bar{\varphi}$  = Average flux, n/cm<sup>2</sup>/sec

U, Pu

$\sum_i$  = Summation over the heavy isotopes uranium and plutonium

$\delta k$  = Reactivity effect

$\sum \delta k_j$  = Summation of reactivity effects by energy group  $j$

$\nabla \varphi_j$  = Gradient of the real flux in energy group  $j$

$\nabla \varphi_j^+$  = Gradient of the adjoint flux in energy group  $j$





# COMPARISON OF THE VARIOUS NEUTRONIC REPRESENTATIONS FOR EBR-II ANALYSES

by

J. T. Madell and R. E. Jarka

## ABSTRACT

This report presents and evaluates the methods of preparing the input specifications for neutronic analyses of EBR-II. The input specifications for one- and two-dimensional calculations include regional designations, volume fractions, atomic densities, and mesh intervals. The production, collapsing, and analyses of various cross-section sets are discussed.

EBR-II loadings with steel and depleted-uranium subassemblies in the inner blanket were simulated for one- and two-dimensional calculations.

The influence of diffusion and transport approximations and of several cross-section sets on neutronic quantities of these loadings is investigated for one- and two-dimensional calculations. The neutronic quantities obtained from various one-dimensional representations are compared to those obtained from a two-dimensional representation.

## I. INTRODUCTION

The reactor-physics analysis of EBR-II has been extensively documented<sup>1-3</sup> from the initial critical experiments in the mid-1950's to the approach to power in July 1964. During this period, the overall objective of EBR-II was to demonstrate the operation of a fast-breeder-reactor power plant with an integrated fuel-reprocessing facility. However, the initial design purpose of EBR-II has changed to that of an irradiation facility for the LMFBR program.

Concurrent with this change in its purpose, there have been significant physical changes in EBR-II. For example, the fuel (Mark IA) is shorter (13.5 in. compared with a previous 14.2 in.) and is more highly enriched than that in the initial loading (~52.5 at. % compared with a previous 48 at. %). The upper and lower axial blankets of depleted-uranium pins were changed to reflectors with steel pins and then to

trifluted steel reflectors. Experimental subassemblies have been added to the core and inner-blanket regions. Their number has increased over the past three years to about 15 in the core and an additional four or five in the inner blanket. The total number of subassemblies in the core has increased from 70 in the wet critical experiments<sup>4</sup> to 91 that now completely fill the first six rows. The steady-state operating power has increased during 1968 from 45 to 50 MWt. Occasionally EBR-II has operated with as few as 10 control rods, as compared with 12 in the early stage of operation.

From run 25 to run 29A, a steel reflector subassembly replaced the depleted-uranium subassemblies in the inner radial blanket. A fuel driver subassembly of a third design, designated Mark II, is being irradiated on an experimental basis. Numerous other changes being considered include control rods with a  $B_4C$  poison section, nickel reflector subassemblies for the inner blanket, and the placement of driver subassemblies in the seventh row of the core.

Changes during the last three years have required a renewal of the reactor-physics analysis of EBR-II. The purpose of this analysis has been to provide data for the design of new components and for understanding reactor characteristics after changes in loading.

New tools for the reactor analysis had to be adapted and developed. The computer programs used 10 years ago were not recoded for the new computers, and the codes themselves have become obsolete, because the new techniques in problem solving allow more versatile, faster, and more accurate solutions. Also, neutron cross-section data have improved greatly as have the methods of preparing these data for neutronic codes.

This report presents many of the current methods: (1) representing the physical components of EBR-II in the neutronic calculation, (2) preparing the neutron cross sections, and (3) employing the various one- and two-dimensional neutronic codes. The purpose of this report is to compare the results obtained from applying various of these representations, cross sections, and neutronic codes to the EBR-II.

## II. REPRESENTATION OF THE PHYSICAL SYSTEM FOR NEUTRONIC CALCULATIONS

### A. Introduction

For a neutronic calculation of a reactor, a physical description of the reactor must be provided as input information to the computer code. The input data include overall dimensions of the system, a definition of homogeneous material regions in the reactor, and the dimension and composition of these regions. For codes that use a finite-difference method of solution, a mesh interval is also specified.

A knowledge of the physical arrangement of EBR-II is required before specifying the input data for computer codes. EBR-II is composed

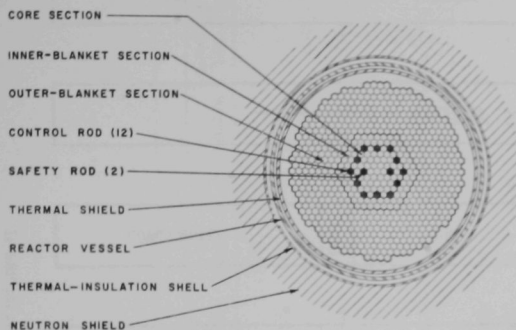


Fig. 1. Horizontal Section of EBR-II.  
ANL Neg. No. 111-5096.

of hexagonally shaped sub-assemblies, standing vertically in a closely packed array. Figure 1 shows a horizontal section of the core and blanket arrangement. All subassemblies, both in the core and blanket regions, have identical external dimensions; thus the subassembly serves as the basic unit in describing EBR-II for calculations. Core sub-assemblies are divided into five axial regions, and blanket subassemblies are simulated by one axial region. No sub-assemblies are divided into

radial or horizontal material regions; thus none of the heterogeneous structure in a fuel subassembly of fuel pins, sodium bond, steel cladding, sodium coolant, and subassembly steel wrapper are represented in the calculations cited here. The composition and dimensions of a region are obtained from the composition and uniform dimensions of the subassemblies enclosed in the region. The various types of EBR-II subassemblies are described in Section B below.

## B. Types of Subassemblies

Fourteen types of subassemblies presently are or previously have been loaded into EBR-II. Changes in the loadings of EBR-II are illustrated by the various types of core subassemblies. Two types of fuel and three designs of the axial blanket combine to form eight types of driver, control, and safety subassemblies. Also included in the 14 types of subassemblies are half-loaded subassemblies (containing 46 fuel pins and 45 steel pins), a subassembly containing an oscillator, and another with a steel drop-rod for dynamic measurements. The design details of the subassemblies are available from engineering drawings of the EBR-II Project, and Fig. 2 illustrates the dimensions at 700°F and the material regions of various types of subassemblies. Table I gives the volume fractions of fuel (uranium-5 wt % fission), steel, and sodium for 14 subassemblies. Since all core-type subassemblies are required to fit the five-axial-region representation, the number of regions in some types of subassemblies must be reduced to five. For example, the sodium space and upper reflector regions of a control or safety subassembly are combined to form the upper reflector region.

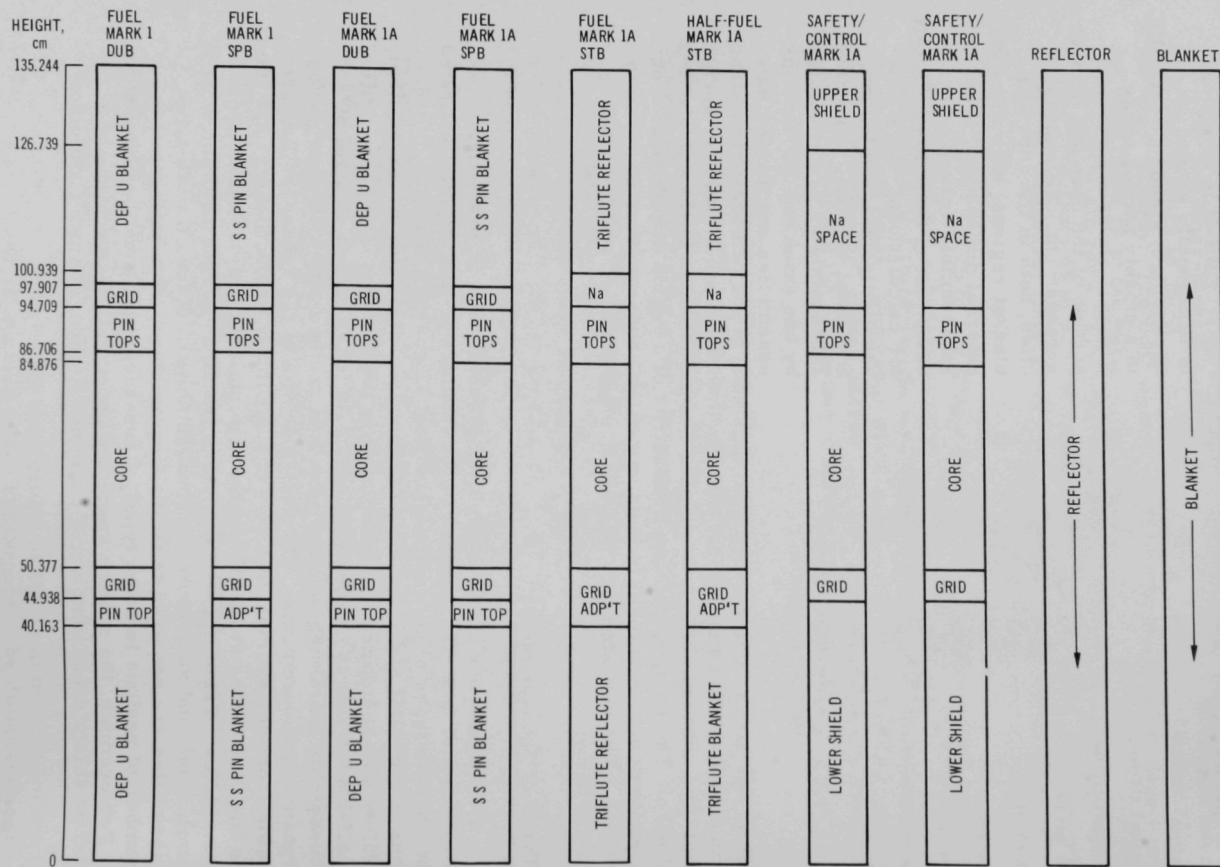


Fig. 2. Regional and Dimensional Description of Various Types of Subassemblies for EBR-II

TABLE I. Material Volume Fractions in the 14 Types of Subassemblies for EBR-II

Region	Material	Subassembly Type/Design												Experiment/ Mark IAC	Fuel/ Mark II
		Fuel <sup>a</sup> / Mark I	Fuel <sup>b</sup> / Mark I	Fuel <sup>a</sup> / Mark IA	Fuel <sup>b</sup> / Mark IA	Fuel <sup>c</sup> / Mark IA	Half-loaded Fuel <sup>c</sup> /Mark IA	Control and Safety/Mark I	Control and Safety/Mark IA	Reflector	Blanket	Dummy	Oscillator		
Upper blanket or reflector	U (dep)	0.279	-	0.279	-	-	-	-	-	-	0.600	-	-	-	-
	SS	0.222	0.488	0.212	0.491	0.530	0.530	0.182	0.182	0.809	0.176	0.182	0.182	0.588	0.641
	Na	0.509	0.512	0.509	0.509	0.470	0.470	0.818	0.818	0.191	0.224	0.818	0.818	0.412	0.359
Pin tops	SS	0.351	0.351	0.432	0.432	0.432	0.474	0.282	0.347	0.899	d	0.109	0.109	0.588	0.253
	Na	0.394	0.394	0.485	0.485	0.485	0.485	0.482	0.593	0.191	d	0.891	0.891	0.412	0.454
Core	Fuel	0.3437 <sup>e</sup>	0.3437 <sup>e</sup>	0.3263	0.3263	0.3263	0.1632	0.2245 <sup>e</sup>	0.2131	-	d	-	f	f	0.2532
	(Uranium)	(0.3100)	(0.3100)	(0.2943)	(0.2943)	(0.2943)	(0.1472)	(0.2025)	(0.1922)	-	d <sup>g</sup>	-	f	f	(0.2284)
	(Fissium)	(0.0337)	(0.0337)	(0.0320)	(0.0320)	(0.0320)	(0.0160)	(0.0220)	(0.0209)	-	d	-	f	f	(0.0248)
	SS	0.2090	0.2090	0.1984	0.1984	0.1984	0.3616	0.2047	0.1944	0.809	d	0.550	f	f	0.216
	Na	0.5006	0.5006	0.4753	0.4753	0.4753	0.4753	0.6241	0.5925	0.191	d	0.450	f	f	0.532
Pin grid	SS	0.314	0.440	0.314	0.440	0.550	0.550	0.553	0.553	0.809	d	0.553	0.553	0.550	0.550
	Na	0.576	0.560	0.576	0.560	0.450	0.450	0.447	0.447	0.191	d	0.447	0.447	0.450	0.450
Lower blanket or reflector	U (dep)	0.303	-	0.303	-	-	-	-	-	-	0.600	-	-	-	-
	SS	0.185	0.488	0.185	0.488	0.615	0.615	0.553	0.553	0.809	0.176	0.553	0.553	0.615	0.641
	Na	0.512	0.512	0.512	0.512	0.385	0.385	0.447	0.447	0.191	0.224	0.447	0.447	0.385	0.359

<sup>a</sup>Depleted-uranium blanket.<sup>b</sup>Steel pin blanket.<sup>c</sup>Steel tritute blanket.<sup>d</sup>These regions do not occur in the blanket subassembly.<sup>e</sup>Volume fractions adjusted to Mark-IA dimensions.<sup>f</sup>Atomic densities provided by EBR-II staff.

The geometrical representation of EBR-II must be consistent with the geometries allowed by the neutronic codes. The available codes used for this work allow cylindrical, slab, and spherical representations. In the radial direction, EBR-II, which is composed of hexagonally shaped subassemblies on a triangular pitch, is represented in one dimension by either a cylindrical or a spherical geometry. A slab geometry is used to represent EBR-II in the axial direction. For two-dimensional calculations, both  $(r,z)$  and  $(x,y)$  simulations are used for EBR-II.

### C. Radial Representation of EBR-II

In the radial direction, the regional representation depends on the loading arrangement of the various types of subassemblies. When EBR-II was composed only of fuel and depleted-uranium subassemblies, the reactor could be represented by one core region and one blanket region in the radial direction. Additional regions may be used to represent the more lightly fueled safety and control subassemblies. However, recent increases in the types of subassemblies in EBR-II have resulted in a greater variation of the material composition within the core and have necessitated an investigation of the regional representation, particularly in the radial direction.

The subassemblies are arranged in hexagonally shaped rows. In the simplest model, each hexagonal row of the core can be represented as an annular ring for neutronic calculations. Because the inner and outer blankets are sufficiently homogeneous, each is represented as a single annular region. Figure 3 shows the approximate nature of the model and the difference between an annular ring and a hexagonal row. The difference in the representations increases with distance from the reactor center; however, the neutronic importance of an accurate representation decreases with distance. A more accurate representation of the radial regions has been developed.<sup>5</sup> In this representation, the core is divided into 15 annular regions. The fraction of each subassembly that resides in a given annular region is calculated here exactly from geometrical relationships and totaled

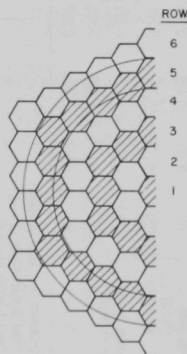


Fig. 3

Hexagonal Rows of EBR-II Subassemblies  
with Annular Region for Fifth Row. ANL  
Neg. No. 113-1486.

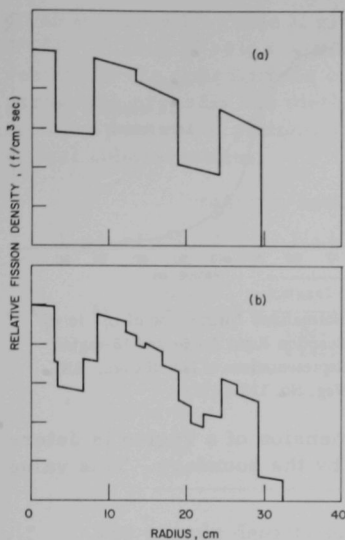


Fig. 4. Fission Densities for 6- and 15-region Representations of EBR-II Core. ANL Neg. No. 113-1477.

distribution. However, in future loadings the core will probably become less homogeneous; that is, more types of subassemblies and greater diversity of materials will be added. Consequently, the model of regional representation requires periodic review.

to give the homogeneous composition of each of the 15 regions. Thus the radial distance of the fuel from the core center is more accurately reproduced in this representation. Diffusion-theory calculations<sup>6</sup> have been performed in one-dimensional, cylindrical geometry using the two models for the identical loading. The calculated eigenvalues are almost identical and differ by only 0.0004. The significant differences in density distributions, shown in Fig. 4, result from differences in the homogenized regional compositions. However, the reaction-rate distributions of  $\sigma_f^{25}\phi$ ,  $\sigma_c^{25}\phi$ ,  $\sigma_f^{28}\phi$ , and  $\sigma_f^{28}\phi/\sigma_f^{25}\phi$  are in good agreement for both models, as shown in Figs. 5-8, respectively.

For the arrangement of subassemblies in the run-25 loading of EBR-II, the simple model of six annular regions for the core is sufficient to obtain the eigenvalue and neutronic characteristics dependent only on the neutron spectrum and

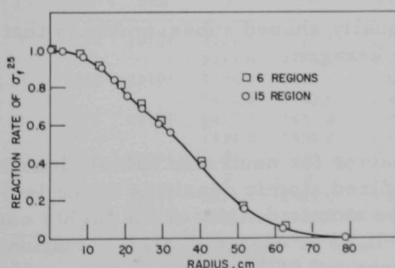


Fig. 5. Normalized Distribution of  $\sigma_f^{25}$  Reaction Rate for 6- and 15-region Representations of EBR-II Core. ANL Neg. No. 113-1510.

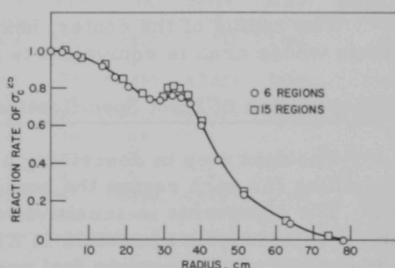


Fig. 6. Normalized Distribution of  $\sigma_c^{25}$  Reaction Rate for 6- and 15-region Representations of EBR-II Core. ANL Neg. No. 113-1500.



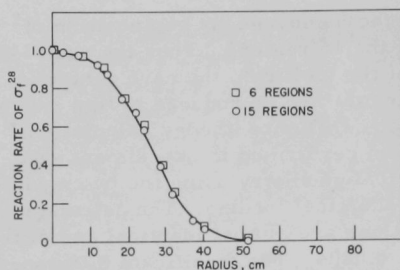


Fig. 7. Normalized Distribution of  $\sigma_f^{28}$  Reaction Rate for 6- and 15-region Representations of EBR-II Core. ANL Neg. No. 113-1509.

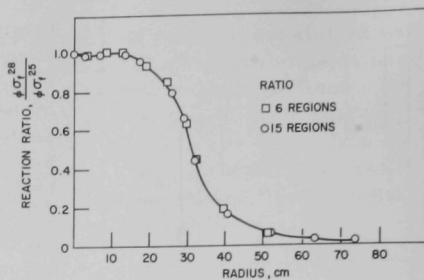


Fig. 8. Normalized Distribution of  $\sigma_f^{28}$  to  $\sigma_f^{25}$  Reaction Ratio for 6- and 15-region Representations of EBR-II Core. ANL Neg. No. 113-1476.

From the simple model, the radial dimension of a region is determined from the total subassemblies enclosed by the boundary. This value is calculated by

$$r = r_0 \sqrt{N}, \quad (1)$$

where

$r_0$  = the radius of the center subassembly, cm,

and

$N$  = the total number of subassemblies enclosed within the radius  $r$ .

The radius of the center, hexagonally shaped subassembly is that of a circle whose area is equivalent to the hexagon.

#### D. Preparation of Input Specifications

The next step in describing a reactor for neutronic calculations is to calculate for each region the homogenized atomic densities of the isotopes. The eigenvalue is sensitive to the atomic density of the highly concentrated fissionable materials in EBR-II. For example, a 1% variation in the density of the uranium fuel produces a 0.55% variation in the value of  $k_{eff}$ . Early calculations of EBR-II showed the necessity of developing an accurate, systematic method to obtain the atomic densities of materials for the various loadings of EBR-II. As for the geometrical representation, the procedure starts with the isotopic concentrations within the basic unit of a subassembly; then the isotopic concentrations of the subassemblies in a region are combined to give the atomic densities for that region. Table I gives the volume fractions of all materials (depleted uranium, stainless steel, and sodium) for the 14 types of subassemblies in all regions except the core regions. The volume fractions of steel, fissium, and sodium in the core region of all but experimental and oscillator subassemblies also are

given in Table I. Table II gives the atomic densities of these materials at 700°F. A lack of cross-section data for some of the isotopes in fissium results in the approximate compositions given in Table II. The following paragraph presents the method of calculating the atomic densities of heavy isotopes (uranium, plutonium, and fission-product pairs) in the core region of fuel subassemblies.

TABLE II. Atomic Densities of Depleted Uranium, Steel, and Fissium at 700°F

Nuclide	Densities, $10^{24}$ atoms/cm <sup>3</sup>		
	Natural Uranium	Steel	Fissium
<sup>235</sup> U	$1.024 \times 10^{-4}$		
<sup>238</sup> U	$4.6441 \times 10^{-2}$		
Fe		$6.002 \times 10^{-2}$	
Ni		$7.599 \times 10^{-3}$	
Cr		$1.7151 \times 10^{-2}$	
Mo			$2.5697 \times 10^{-2}$
Nb			$1.0362 \times 10^{-4}$
Zr			$2.1035 \times 10^{-2}$

The atomic density of the heavy isotopes for each fuel subassembly is calculated by the HVYISO code, programmed for the CDC-160A computer. The input data are provided in the form of a computer listing that gives the type of subassembly in each core position, the original and final weights ( $W_0$  and  $W_f$ ) of the heavy isotopes (<sup>235</sup>U, <sup>238</sup>U, and <sup>239</sup>Pu), and the percent burnup, BU, for every subassembly in each EBR-II loading. Table III

TABLE III. Partial Computer Listing of Loading Data for Run 26  
Run 26.2 (1028 MWD) 13894 to 14922 MWD

TY	No	Pos	235	238	236	239	Fz	B-AX	B-MX	MWD	MWDL
1	283	10101	2717.5	2761.6	16.0	8.4	358	1.0660	1.1992	3307	2
			2784.0	2768.3	4.7	5.8	299	0	0		
1	298	20101	1375.9	1400.6	6.8	0.7	177	0.8255	0.9329	2680	774
			1402.0	1403.0	2.4	0	154	0	0		
1	298	20101	1412.2	1432.8	6.9	0	102	0.0268	0.9343	2680	769
			1439.0	1435.2	2.4	0	158	0	0		
1	9018	20201	0	0	0	0	0	0	0	3307	86693
			0	0	00	0	0	0	0		
1	292	20301	2829.3	2669.0	13.8	6.3	347	0.8538	0.9648	2680	659
			2883.0	2674.3	4.7	4.7	300	0	0		

TY: Type of subassembly.

No: Number of the subassembly.

Pos: Location in reactor (row/segment/position).

235: Weight of <sup>235</sup>U, g.

238: Weight of <sup>238</sup>U, g.

236: Weight of <sup>236</sup>U, g.

239: Weight of <sup>239</sup>Pu, g.

Fz: Weight of fissium and FPP, g.

B-AX: Average burnup.

B-MX: Maximum burnup.

MWD: Total exposure in megawatt-days.

MWDL: Remaining exposure to reach specified burnup in MWD.

First line refers to quantity at end of run.

Second line refers to quantity at time of initial insertion.

illustrates an example of a computer listing. With these data, the code computes the atomic density,  $\rho_i$ , of the  $i$ th heavy isotope for each subassembly and then combines the atomic densities of the subassemblies in the region. Additional input to HVIISO consists of Avogadro's number,  $A_0$ , the atomic weight  $(AW)_i$ , of the  $i$ th heavy isotope, and the volume,  $V$ , of the subassembly core region (constant for all subassemblies) at  $700^\circ\text{F}$ , and the number of subassemblies in a given region,  $M$ . The value of  $\rho_i^R$  for the  $R$ th region is obtained by calculating

$$\rho_i^R = \frac{A_0 \sum_i^N W_i^n}{(AW)_i V} \text{ atoms/cm}^3. \quad (2)$$

The atomic densities of the fission-product pairs are not given directly in the computer listing but rather are computed as

$$\rho_{\text{FPP}} = \sum_i^{U, \text{Pu}} \rho_{i_0} \cdot \text{BU}, \quad (3)$$

where the subscript 0 refers to the initial atomic density of the  $i$ th heavy isotope. The atomic densities of the heavy isotopes are printed out for each subassembly and for each core region; the results are also punched on data-processing cards in the standard ANL format.<sup>7</sup>

As was mentioned earlier in this section, the atomic densities of the nuclides in the core section of experimental and oscillator subassemblies are treated separately. The weights of the heavy isotopes and of other materials in an experimental subassembly are provided by the ANL-Idaho staff from the experimenter's specifications. The weights are converted into atomic densities, which in turn are combined in the appropriate homogeneous regions. The portion of the oscillator in the core region consists of boron, steel, and sodium. The atomic densities of each material are calculated and incorporated into the appropriate region, in the same method used for the materials in the experimental subassemblies.

The volume fractions of the steel, sodium, fissium, and depleted uranium in each subassembly are then combined by the COMPOS code to yield the homogeneous composition of these materials for the appropriate regions. COMPOS, which is also programmed on the CDC-160A, inputs the data on (1) volume fractions given in Table I, (2) the number and types of subassemblies in each region, and (3) the regional assignments of the atomic densities of the heavy isotopes (which were obtained by the HVIISO code) and of the experimental materials. The code combines the appropriate data for each region, calculates the volume fraction of the materials in each region, and assigns a composition number to the material combination. The data are listed and also punched on cards in the standard ANL input format.

The selection of the number of mesh intervals depends on the types of information desired from the calculation and on the storage limitation of the particular neutronic program. For calculation of the eigenvalue and of other integral quantities by one-dimensional codes, mesh intervals of about 1 cm in the core and of about 2 cm in the blanket and reflector regions have given satisfactory results. The storage limitations and consideration of computation time of the two-dimensional code have resulted in selecting ~2-cm mesh intervals for the core regions and ~3-cm mesh intervals for the reflector and blanket regions.

Smaller mesh intervals in a specific region have been used for a detailed analysis of that region. For example, the power distribution near interface between the core and the radial blanket changes greatly with position; therefore, a mesh interval of less than 1 cm is required to calculate this quantity accurately.

### III. NEUTRON CROSS-SECTION SETS

#### A. Development of Sets 236, 23606, 23605, 238, 23806, and JM31F

The tools of reactor analysis have changed greatly in the last 10 years, and the change is most evident in the area of neutron cross sections. In fact, there has even been a significant change in the availability of basic cross-section data during the period of this work. In all, six cross-section sets were developed for this analysis of EBR-II. These are described in the following paragraphs in the chronological order of their development. Details of the development of the cross-section sets are contained in Refs. 8 and 9.

##### 1. Set 236

Cross-section set 236 was generated<sup>10</sup> by MC<sup>2</sup> in January 1967. The MC<sup>2</sup> library tape at that time was a limited edition of the one used<sup>11</sup> for generating set 224. Weighting spectra characteristic of the run-20 core loading of EBR-II and of the depleted uranium blanket were used to generate the 22-energy group set used in this study. A value of  $B^2 = 0$  was assumed in calculating the cross sections for the core and blanket. The MC<sup>2</sup> library tape did not contain any data on (n,p), (n,2n), or (n, $\alpha$ ) reactions. Table IV gives the energy structure and the nuclides with their weighting spectra. The cross sections for some nuclides absent from the MC<sup>2</sup> library tape were obtained from set 224, and these are identified by the weighting spectrum in Table IV. The MC<sup>2</sup> output was converted to both XLIBIT and MACHLIB formats in which the number of down-scatter groups was limited to 12.

TABLE IV. Description of Cross-section Set 236

Energy Group	Lower Energy Limit, eV	Upper Lethargy Limit	Nuclide Number	Nuclide	Remarks
1	$3.68 \times 10^6$	1.0	1	$^{235}\text{U}$	EBR-II core spectrum weighted
2	$2.23 \times 10^6$	1.5	2	$^{239}\text{Pu}$	
3	$1.35 \times 10^6$	2.0	3	$^{238}\text{U}$	
4	$8.21 \times 10^5$	2.5	4	Fe	
5	$4.98 \times 10^5$	3.0	5	Ni	
6	$3.02 \times 10^5$	3.5	6	Cr	
7	$1.83 \times 10^5$	4.0	7	Na	
8	$1.11 \times 10^5$	4.5	8	Fission-product pairs	
9	$6.74 \times 10^4$	5.0	9	$^{235}\text{U}$	EBR-II blanket spectrum weighted
10	$4.09 \times 10^4$	5.5		$^{239}\text{Pu}$	
11	$2.48 \times 10^4$	6.0		$^{238}\text{U}$	
12	$1.50 \times 10^4$	6.5		Fe	
13	$9.12 \times 10^3$	7.0		Ni	
14	$4.31 \times 10^3$	7.75		Cr	
15	$2.62 \times 10^3$	8.25		Na	
16	$2.03 \times 10^3$	8.50		Mo	
17	$1.23 \times 10^3$	9.0	17	Nb	Cross sections from set 224
18	$9.61 \times 10^2$	9.25		Zr	
19	$5.83 \times 10^2$	9.75		B(NAT.)	
20	$2.75 \times 10^2$	10.5		C	
21	$1.01 \times 10^2$	11.5		O	
22	$2.90 \times 10^1$	12.75		W	
				Ta	
				$^{10}\text{B}$	

The MC<sup>2</sup> calculations that produced the cross sections for all 22-group sets (236, 238, and JM31F) used the ordinary P1 approximation for the fundamental-mode weighting spectrum. Thus, the scattering cross sections were obtained by the same approximation used by diffusion theory; all scattering cross sections are assumed to be isotropic in the center-of-mass system and are then corrected by translating to the center-of-laboratory systems. Only isotopic scattering cross sections were used in the transport, as well as diffusion-theory, calculations presented here.

## 2. Set 23606

Cross-section set 23606 is a six-group set obtained by collapsing 22-group set 236. A set with six groups or less allows calculations on CANDID-2D<sup>12</sup> and SNARG-2D<sup>13</sup> to run within an acceptable amount of computer time. For example, a six-group, 1200-mesh-point, two-dimensional SNARG problem takes 60-90 min with no inputted flux.

Set 23606 was generated in MACHLIB and XLIBIT formats by the group-collapsing routine of the MACH-1 code<sup>6</sup> that performs a linear-flux weighting. The spectra used for the collapsing to set 23606 were obtained from the volume-averaged fluxes of a MACH-1 spherical representation

of the EBR-II, run 20 core and blanket regions. The transport cross sections for all collapsed sets were obtained by averaging the 22-group transport cross sections ( $\Sigma_{tr}$  weighting) rather than the inverse of the 22-group  $\Sigma_{tr}$ 's (D weighting). The energy group structure for the set was obtained by a trial-and-error method, and the results of calculations using set 236 were compared to those using trial six-group structures. The set 23606 group structure resulting from this procedure is included in Table V, with the nuclide identification and its weighting spectrum. The final group structure yielded excellent agreement between the particular perturbation results using sets 236 and 23606, as cited in Table VI. Figure 9 shows excellent agreement of the real and adjoint flux produced by the two cross-section sets.

TABLE V. Description of Cross-section Sets 23606 and 23605

Set 23606					
Energy Group	Corresponding Set 236 Groups	Lower Energy Limit, eV	Upper Lethargy Limit		
1	1, 2	$2.23 \times 10^6$	1.5		
2	3, 4	$8.21 \times 10^5$	2.5		
3	5, 6	$3.02 \times 10^5$	3.5		
4	7, 8	$1.11 \times 10^5$	4.5		
5	9, 10	$4.09 \times 10^4$	5.5		
6	11-22	$2.90 \times 10$	12.75		

Nuclide Number	Nuclide	Weighting Spectrum	Nuclide Number	Nuclide	Weighting Spectrum
1	$^{235}\text{U}$	EBR-II core	14	Cr	EBR-II blanket
2	$^{239}\text{Pu}$	EBR-II core	15	Na	EBR-II blanket
3	$^{238}\text{U}$	EBR-II core	16	Mo	EBR-II core
4	Fe	EBR-II core	17	Nb	EBR-II core
5	Ni	EBR-II core	18	Zr	EBR-II core
6	Cr	EBR-II core	19	B(NAT.)	EBR-II core
7	Na	EBR-II core	20	C	EBR-II core
8	Fission-product pairs	EBR-II core	21	O	EBR-II core
9		EBR-II core	22	W	EBR-II core
10	$^{235}\text{U}$	EBR-II blanket	23	Ta	EBR-II core
11	$^{239}\text{Pu}$	EBR-II blanket	24	$^{10}\text{B}$	EBR-II core
12	$^{238}\text{U}$	EBR-II blanket	25	EBR-II core	-
13	Fe	EBR-II blanket	26	EBR-II blanket	-
	Ni	EBR-II blanket			

Set 23605			
Energy Group	Corresponding Set 236 Groups	Lower Energy Limit, eV	Upper Lethargy Limit
1	1, 2, 3	$1.35 \times 10^6$	2.0
2	4, 5	$4.98 \times 10^5$	3.0
3	6, 7	$1.83 \times 10^5$	4.0
4	8, 9	$6.74 \times 10^4$	5.0
5	10-22	$2.90 \times 10$	12.75

Nuclide number, name, and corresponding weighting spectrum for set 23605 are the same as those for set 23606.

TABLE VI. Reactivity Worths of Various Materials due to a 1% Decrease in Density as Calculated by Cross-section Sets 236, 23606, and 23605

Nuclide	$\Delta k/k/\Delta V$ Terms	Region 1 (Row 1)			Region 2 (Rows 2, 3, and 4)			Region 3 (Rows 5 and 6)		
		236	23605	23606	236	23605	23606	236	23605	23606
$^{235}\text{U}$	Source	$-2.91 \times 10^{-7}$	$-2.93 \times 10^{-7}$	$-2.93 \times 10^{-7}$	$-1.98 \times 10^{-7}$	$-1.99 \times 10^{-7}$	$-1.99 \times 10^{-7}$	$-1.11 \times 10^{-7}$	$-1.11 \times 10^{-7}$	$-1.11 \times 10^{-7}$
	C + F	$1.40 \times 10^{-7}$	$1.41 \times 10^{-7}$	$1.41 \times 10^{-7}$	$9.51 \times 10^{-8}$	$9.56 \times 10^{-8}$	$9.57 \times 10^{-8}$	$5.18 \times 10^{-8}$	$5.17 \times 10^{-8}$	$5.18 \times 10^{-8}$
	Leak	$-1.33 \times 10^{-10}$	$-1.33 \times 10^{-10}$	$-1.34 \times 10^{-10}$	$-3.86 \times 10^{-9}$	$-3.86 \times 10^{-9}$	$-3.90 \times 10^{-9}$	$-6.34 \times 10^{-9}$	$-6.34 \times 10^{-9}$	$-6.42 \times 10^{-9}$
	Scat	$-2.34 \times 10^{-10}$	$-1.89 \times 10^{-9}$	$-2.17 \times 10^{-9}$	$-1.03 \times 10^{-9}$	$0.77 \times 10^{-9}$	$-0.95 \times 10^{-9}$	$1.90 \times 10^{-10}$	$2.65 \times 10^{-10}$	$1.96 \times 10^{-10}$
	Total	$-1.53 \times 10^{-7}$	$-1.54 \times 10^{-7}$	$-1.54 \times 10^{-7}$	$-1.08 \times 10^{-7}$	$-1.08 \times 10^{-7}$	$-1.09 \times 10^{-7}$	$-6.53 \times 10^{-8}$	$-6.51 \times 10^{-8}$	$-6.53 \times 10^{-8}$
$^{238}\text{U}$	Source	-	+0.6	+0.6	-	0.0	+0.9	-	-0.5	0.0
	C + F	$-2.22 \times 10^{-8}$	$-2.22 \times 10^{-8}$	$-2.21 \times 10^{-8}$	$-1.43 \times 10^{-8}$	$-1.43 \times 10^{-8}$	$-1.43 \times 10^{-8}$	$-6.57 \times 10^{-9}$	$-6.54 \times 10^{-9}$	$-6.61 \times 10^{-9}$
	Leak	$2.00 \times 10^{-8}$	$2.02 \times 10^{-8}$	$2.01 \times 10^{-8}$	$1.35 \times 10^{-8}$	$1.35 \times 10^{-8}$	$1.34 \times 10^{-8}$	$7.05 \times 10^{-9}$	$7.04 \times 10^{-9}$	$7.04 \times 10^{-9}$
	Scat	$-1.24 \times 10^{-10}$	$-1.25 \times 10^{-10}$	$-1.26 \times 10^{-10}$	$-3.60 \times 10^{-9}$	$-3.61 \times 10^{-9}$	$-3.64 \times 10^{-9}$	$-5.89 \times 10^{-9}$	$-5.91 \times 10^{-9}$	$-5.96 \times 10^{-9}$
	Total	$-4.74 \times 10^{-10}$	$-0.97 \times 10^{-10}$	$-7.34 \times 10^{-10}$	$2.19 \times 10^{-10}$	$4.35 \times 10^{-10}$	$-0.03 \times 10^{-10}$	$8.05 \times 10^{-10}$	$8.63 \times 10^{-10}$	$6.36 \times 10^{-10}$
Fe	Source	$-2.74 \times 10^{-9}$	$-2.26 \times 10^{-9}$	$-2.92 \times 10^{-9}$	$-4.23 \times 10^{-9}$	$-3.96 \times 10^{-9}$	$-4.46 \times 10^{-9}$	$-4.60 \times 10^{-9}$	$-4.55 \times 10^{-9}$	$-4.89 \times 10^{-9}$
	C + F	-	-17.4	+6.6	-	-6.7	+5.4	-	-1.3	+6.3
	Leak	$9.10 \times 10^{-10}$	$9.16 \times 10^{-10}$	$9.17 \times 10^{-10}$	$6.31 \times 10^{-10}$	$6.32 \times 10^{-10}$	$6.34 \times 10^{-10}$	$3.60 \times 10^{-10}$	$3.58 \times 10^{-10}$	$3.60 \times 10^{-10}$
	Scat	$-9.44 \times 10^{-11}$	$-9.48 \times 10^{-11}$	$-9.49 \times 10^{-11}$	$-2.76 \times 10^{-9}$	$-2.76 \times 10^{-9}$	$-2.77 \times 10^{-9}$	$-4.57 \times 10^{-9}$	$-4.59 \times 10^{-9}$	$-4.58 \times 10^{-9}$
	Total	$1.62 \times 10^{-10}$	$-0.98 \times 10^{-10}$	$1.83 \times 10^{-10}$	$4.02 \times 10^{-10}$	$2.13 \times 10^{-10}$	$3.84 \times 10^{-10}$	$5.88 \times 10^{-10}$	$4.66 \times 10^{-10}$	$5.43 \times 10^{-10}$
Ni	Source	$9.77 \times 10^{-10}$	$7.23 \times 10^{-10}$	$10.05 \times 10^{-10}$	$-1.72 \times 10^{-9}$	$-1.92 \times 10^{-9}$	$-1.75 \times 10^{-9}$	$-3.62 \times 10^{-9}$	$-3.77 \times 10^{-9}$	$-3.68 \times 10^{-9}$
	C + F	-	-26.1	+2.8	-	+11.3	+1.7	-	+4.1	+1.6
	Leak	$7.71 \times 10^{-10}$	$7.63 \times 10^{-10}$	$7.72 \times 10^{-10}$	$5.08 \times 10^{-10}$	$4.99 \times 10^{-10}$	$5.08 \times 10^{-10}$	$2.49 \times 10^{-10}$	$2.42 \times 10^{-10}$	$2.47 \times 10^{-10}$
	Scat	$-1.73 \times 10^{-10}$	$-1.74 \times 10^{-10}$	$-1.75 \times 10^{-10}$	$-4.96 \times 10^{-10}$	$-4.98 \times 10^{-10}$	$-5.03 \times 10^{-10}$	$-7.93 \times 10^{-10}$	$-8.00 \times 10^{-10}$	$-8.07 \times 10^{-10}$
	Total	$-1.22 \times 10^{-10}$	$-1.07 \times 10^{-10}$	$-1.09 \times 10^{-10}$	$-4.44 \times 10^{-11}$	$-3.13 \times 10^{-11}$	$-3.39 \times 10^{-11}$	$3.81 \times 10^{-11}$	$4.43 \times 10^{-11}$	$3.77 \times 10^{-11}$
Cr	Source	$6.32 \times 10^{-10}$	$6.38 \times 10^{-10}$	$6.46 \times 10^{-10}$	$-3.18 \times 10^{-11}$	$-2.99 \times 10^{-11}$	$-2.94 \times 10^{-11}$	$-5.06 \times 10^{-10}$	$-5.14 \times 10^{-10}$	$-5.23 \times 10^{-10}$
	C + F	-	+0.8	+2.2	-	-6.0	-8.2	-	+1.8	+3.4
	Leak	$2.38 \times 10^{-10}$	$2.40 \times 10^{-10}$	$2.40 \times 10^{-10}$	$1.63 \times 10^{-10}$	$1.64 \times 10^{-10}$	$1.65 \times 10^{-10}$	$9.22 \times 10^{-11}$	$9.17 \times 10^{-11}$	$9.20 \times 10^{-11}$
	Scat	$-2.90 \times 10^{-11}$	$-2.86 \times 10^{-11}$	$-2.95 \times 10^{-11}$	$-8.46 \times 10^{-10}$	$-8.35 \times 10^{-10}$	$-8.63 \times 10^{-10}$	$-1.41 \times 10^{-9}$	$-1.39 \times 10^{-9}$	$-1.44 \times 10^{-9}$
	Total	$1.35 \times 10^{-10}$	$0.09 \times 10^{-10}$	$1.10 \times 10^{-10}$	$1.71 \times 10^{-10}$	$0.85 \times 10^{-10}$	$1.45 \times 10^{-10}$	$1.93 \times 10^{-10}$	$1.47 \times 10^{-10}$	$1.70 \times 10^{-10}$
Na	Source	$3.44 \times 10^{-10}$	$2.20 \times 10^{-10}$	$3.21 \times 10^{-10}$	$-5.12 \times 10^{-10}$	$-5.86 \times 10^{-10}$	$-5.53 \times 10^{-10}$	$-1.12 \times 10^{-9}$	$-1.15 \times 10^{-9}$	$-1.17 \times 10^{-9}$
	C + F	-	-36.0	-6.7	-	+14.2	+8.0	-	+2.4	+4.5
	Leak	$1.40 \times 10^{-10}$	$1.39 \times 10^{-10}$	$1.41 \times 10^{-10}$	$9.58 \times 10^{-11}$	$9.49 \times 10^{-11}$	$9.60 \times 10^{-11}$	$5.31 \times 10^{-11}$	$5.17 \times 10^{-11}$	$5.22 \times 10^{-11}$
	Scat	$-1.15 \times 10^{-10}$	$-1.17 \times 10^{-10}$	$-1.16 \times 10^{-10}$	$-3.34 \times 10^{-9}$	$-3.40 \times 10^{-9}$	$-3.37 \times 10^{-9}$	$-5.48 \times 10^{-9}$	$-5.59 \times 10^{-9}$	$-5.54 \times 10^{-9}$
	Total	$-2.69 \times 10^{-9}$	$-2.49 \times 10^{-9}$	$-2.26 \times 10^{-9}$	$-1.47 \times 10^{-9}$	$-1.34 \times 10^{-9}$	$-1.15 \times 10^{-9}$	$-2.57 \times 10^{-10}$	$-2.22 \times 10^{-10}$	$-0.49 \times 10^{-10}$
Carbon	Source	$-2.67 \times 10^{-9}$	$-2.47 \times 10^{-9}$	$-2.24 \times 10^{-9}$	$-4.71 \times 10^{-9}$	$-4.65 \times 10^{-9}$	$-4.41 \times 10^{-9}$	$-5.69 \times 10^{-9}$	$-5.76 \times 10^{-9}$	$-5.53 \times 10^{-9}$
	C + F	-	-7.3	-16.1	-	-1.7	-6.4	-	+1.6	-2.8
	Leak	0	0	0	0	0	0	0	0	0
	Scat	$-2.36 \times 10^{-10}$	$-2.37 \times 10^{-10}$	$-2.39 \times 10^{-10}$	$-6.81 \times 10^{-9}$	$-6.85 \times 10^{-9}$	$-6.93 \times 10^{-9}$	$-1.11 \times 10^{-8}$	$-1.12 \times 10^{-8}$	$-1.13 \times 10^{-8}$
	Total	$-1.12 \times 10^{-8}$	$-1.00 \times 10^{-8}$	$-1.05 \times 10^{-8}$	$-6.68 \times 10^{-9}$	$-5.80 \times 10^{-9}$	$-6.10 \times 10^{-9}$	$-1.93 \times 10^{-9}$	$-1.52 \times 10^{-9}$	$-1.52 \times 10^{-9}$
Oxygen	Source	$-1.14 \times 10^{-8}$	$-1.02 \times 10^{-8}$	$-1.08 \times 10^{-8}$	$-1.35 \times 10^{-8}$	$-1.27 \times 10^{-8}$	$-1.30 \times 10^{-8}$	$-1.31 \times 10^{-8}$	$-1.27 \times 10^{-8}$	$-1.29 \times 10^{-8}$
	C + F	-	-10.1	-5.3	-	-6.3	-3.7	-	-2.5	-1.5
	Leak	0	0	0	0	0	0	0	0	0
	Scat	$-4.34 \times 10^{-10}$	$-4.15 \times 10^{-10}$	$-4.46 \times 10^{-10}$	$-1.26 \times 10^{-8}$	$-1.20 \times 10^{-8}$	$-1.30 \times 10^{-8}$	$-2.06 \times 10^{-8}$	$-1.96 \times 10^{-8}$	$-2.16 \times 10^{-8}$
	Total	$-1.57 \times 10^{-8}$	$-0.97 \times 10^{-8}$	$-1.73 \times 10^{-8}$	$-9.20 \times 10^{-9}$	$-5.49 \times 10^{-9}$	$-10.00 \times 10^{-9}$	$-2.62 \times 10^{-9}$	$-1.21 \times 10^{-9}$	$-2.76 \times 10^{-9}$
	Source	$-1.61 \times 10^{-8}$	$-1.01 \times 10^{-8}$	$-1.77 \times 10^{-8}$	$-2.17 \times 10^{-8}$	$-1.75 \times 10^{-8}$	$-2.30 \times 10^{-8}$	$-2.32 \times 10^{-8}$	$-2.08 \times 10^{-8}$	$-2.43 \times 10^{-8}$
	C + F	-	-37.3	+9.9	-	-19.3	+6.0	-	-10.3	+4.7
	Leak	0	0	0	0	0	0	0	0	0
	Scat	$-4.34 \times 10^{-10}$	$-4.15 \times 10^{-10}$	$-4.46 \times 10^{-10}$	$-1.26 \times 10^{-8}$	$-1.20 \times 10^{-8}$	$-1.30 \times 10^{-8}$	$-2.06 \times 10^{-8}$	$-1.96 \times 10^{-8}$	$-2.16 \times 10^{-8}$
	Total	$-1.57 \times 10^{-8}$	$-0.97 \times 10^{-8}$	$-1.73 \times 10^{-8}$	$-9.20 \times 10^{-9}$	$-5.49 \times 10^{-9}$	$-10.00 \times 10^{-9}$	$-2.62 \times 10^{-9}$	$-1.21 \times 10^{-9}$	$-2.76 \times 10^{-9}$

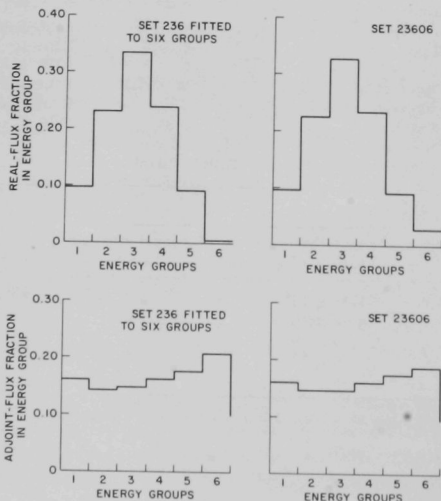


Fig. 9

Comparison of Real- and Adjoint-flux Spectra from Sets 236 and 23606



Two reasons for the excellent representation produced by a six-group set are apparent. First, more than 95% of the flux resides in the first nine of the 22 groups in set 236; since the nine groups are well above the resonance region, the cross sections are smoothly varying and can be accurately collapsed. Second, the adjoint flux is fairly flat over the entire spectrum, and thus no energy regions of high neutron importance require fine energy resolution. Moreover, the same nuclear system (EBR-II, run 20) was the basis for calculating all weighting spectra, the spectra for group collapsing, and the neutronic comparisons, all of which aided in obtaining good comparison between set 236 and the collapsed sets. However, some six-group sets investigated during the trial-and-error procedure gave a poor comparison. If the neutron spectrum is due to changes in the reactor loadings, the energy structure of the six-group set should be reexamined.

### 3. Set 23605

To reduce further the computation times of the neutronic codes, a five-group set (23605) was generated in the same manner as was set 23606. The energy group structure, nuclide identification, and weighting spectrum are given in Table V. The comparisons of the fluxes in Fig. 10 and the reactivity worths in Table VI for sets 236 and 23605 show that the five-group set yields significantly poorer results than does the six-group set.

The major cause for the discrepancies in the perturbation results of the five-, six-, and 22-group sets is usually found to be the inelastic scattering cross sections. The collapsing of a scattering matrix is accomplished in the MACH-1 routine by a linear flux weighting and thus does not take into account the importance of the neutron being scattered from one group into another group of the collapsed energy-group structure. Because the adjoint-flux spectrum is uniform, the magnitude of discrepancies is usually small. The scattering cross sections of light nuclides, such as iron, sodium, etc., are the most difficult to collapse accurately, as is confirmed by the results shown in Table VI.

### 4. Set 238

The neutronic calculations of EBR-II using sets 236 and 23606 predicted eigenvalues and flux distributions that were significantly different (~5%) from measured values.<sup>3</sup> An analysis of these differences, which will be presented in Section III.B, leads to the development of new 22- and six-group cross-section sets. The 22-group cross section, set 238, was generated in the same manner as was set 236, but with the following additions:

- (a) A buckling search was performed by  $MC^2$  for the core composition (a value of  $B^2 = 0$  was used for the blanket and reflector cross sections);
- (b) the compositions used for the weighting spectra were those of run 25;
- (c) cross sections, weighted with a spectrum characteristic of the radial steel reflector were added to the set; and
- (d) use of an edition of  $MC^2$



contained an improved treatment of inelastic scattering. Table VII gives material compositions used in MC<sup>2</sup>; Table VI shows that the energy-group structure is the same as that of set 236; the nuclide identification and the weighting spectrum appear in Table VIII for the MACHLIB and XLIBIT formats.

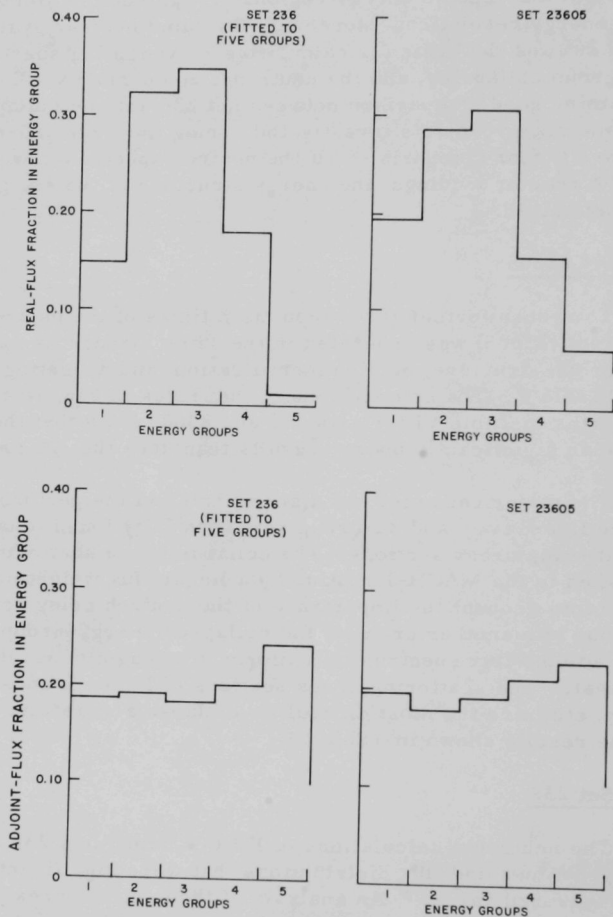


Fig. 10. Comparison of Real- and Adjoint-flux Spectra from Sets 236 and 23605. ANL Neg. No. 112-8815.

TABLE VII. Atomic Densities of Nuclides Used in Generating Weighting Spectra of Set Z38

Nuclide	Core	Blanket	Reflector	Nuclide	Core	Blanket	Reflector
$^{235}\text{U}$	$6.1238 \times 10^{-3}$	$6.6036 \times 10^{-5}$	-	Ni	$1.7365 \times 10^{-3}$	$1.5141 \times 10^{-3}$	$6.1460 \times 10^{-3}$
$^{238}\text{U}$	$5.5760 \times 10^{-3}$	$2.8658 \times 10^{-3}$	-	Cr	$3.9194 \times 10^{-3}$	$3.4173 \times 10^{-3}$	$1.3868 \times 10^{-2}$
$^{239}\text{Pu}$	-	$3.5940 \times 10^{-5}$	-	Na	$1.1176 \times 10^{-2}$	$4.3234 \times 10^{-3}$	$4.3225 \times 10^{-3}$
Fe	$1.3718 \times 10^{-2}$	$1.1960 \times 10^{-2}$	$4.8535 \times 10^{-2}$				

TABLE VIII. Description of Cross-section Sets Z38 and Z3806

Nuclide Designation on Cross-section Tapes						Nuclide Designation on Cross-section Tapes					
Nuclide	Weighting Spectrum	MACHLIB		XLIBIT		Nuclide	Weighting Spectrum	MACHLIB		XLIBIT	
		238	23806	238	23806			238	23806	238	23806
<sup>235</sup> U	C <sup>a</sup>	1	1	U235-C	R-1N-1	Mo	C <sup>a</sup>		12		R-1N34
	R <sup>b</sup>	23	21	U235-R	R-2N23		R <sup>b</sup>		32		R-2N34
	B <sup>c</sup>	12	41	U235-B	R-3N12		B <sup>c</sup>		52		R-3N34
<sup>239</sup> Pu	C	2	2	Pu239C	R-1N-2	Nb	Set Z24	34		MO----	
	R	24	22	Pu239R	R-2N24		C		13		R-1N35
	B	13	42	Pu239B	R-3N13		R		33		R-2N35
<sup>238</sup> U	C	3	3	U238-C	R-1N-3	Zr	B		53		R-3N35
	R	25	23	U238-R	R-2N25		Set Z24	35		NB----	
	B	14	43	U238-B	R-3N14		C		14		R-1N36
<sup>240</sup> Pu	C	4	4	PU240C	R-1N-4	B <sup>nat</sup>	R		34		R-2N36
	R	26	24	PU240R	R-2N26		B		54		R-3N36
	B	15	44	PU240B	R-3N14		Set Z24	36		ZR----	
Fe	C	5	5	FE---C	R-1N-5	W	C		15		R-1N37
	R	27	25	FE---R	R-2N27		R		35		R-2N37
	B	16	45	FE---B	R-3N16		B		55		R-3N37
Ni	C	6	6	NI---C	R-1N-6	Ta	Set Z24	37		BNAT--	
	R	28	26	NI---R	R-2N28		C		16		R-1N38
	B	17	46	NI---B	R-3N17		R		36		R-2N38
Cr	C	7	7	CR---C	R-1N-7	10B	B		56		R-3N38
	R	29	27	CR---R	R-2N29		Set Z24	38		W----	
	B	18	47	CR---B	R-3N18		C		17		R-1N39
Na	C	8	8	NA---C	R-1N-8	Fissium	B		37		R-2N39
	R	30	28	NA---R	R-2N30		B		57		R-3N39
	B	19	48	NA---B	R-3N19		Set Z24	39		TA----	
FPAIR <sup>d</sup>	C	9	9	FPAIRC	R-1N-9	Stainless steel	C		18		R-1N40
	R	31	29	FPAIRR	R-2N31		R		38		R-2N40
	B	20	49	FPAIRB	R-3N20		B		58		R-3N40
<sup>16</sup> O	C	10	10	OXY--C	R-1N10	Set Z24	Set Z24	40		B10---	
	R	32	30	OXY--R	R-2N32		C	41	19		R-1N41
	B	21	50	OXY--B	R-3N21		R	43	39		R-2N43
<sup>12</sup> C	C	11	11	CAR--C	R-1N11	Set Z24	B	42	59		R-3N42
	R	33	31	CAR--R	R-2N33		C		20		R-1N44
	B	22	51	CAR--B	R-3N22		R		40		R-2N44
							B		60		R-3N44
							Set Z24	44			

<sup>a</sup>Core.<sup>b</sup>Reflector.<sup>c</sup>Blanket.<sup>d</sup>Fission-product pair.

5. Set 23806

The six-group cross section, set 23806, was produced by collapsing set 238 in the same manner as set 23606 had been generated from set 236. A comparative study of the eigenvalues calculated, using sets 238 and 23806, indicated good agreement. The set 23606 group structure in Table IV was selected for set 23806 on the basis of a structure analysis of set 23606. Table VIII gives the nuclide identification and weighting spectrum for the MACHLIB and XLIBIT formats. A five-group set was not generated from set 238, because the approximate nature of the energy-group structure was unacceptable.

6. Set JM31F

Analysis of threshold detectors irradiated in EBR-II has shown the need for a finer resolution of the high-energy flux.<sup>14</sup> The strong energy dependence of the neutron cross sections of the threshold detectors above 1 MeV cannot be represented accurately by the three broad groups of set 238. The good resolution of the high-energy flux is important (a) in analyzing the threshold reactions used in the study of radiation damage to materials, and (b) when used as a detector in predicting the magnitude and spectrum of the flux.

A set of 22-group cross sections (set JM31F) has been developed to meet the above need. The energy-group structure in Table IX provides for 16 groups of 1/8 lethargy units between 10 and 2.25 MeV. The 17th, 18th, and 19th groups were selected to correspond to the third, fourth, and fifth groups of set 238. The energy limits of the 20th and 21st groups of set JM31F are identical to those of the fourth and fifth groups of set 23806. The lower energy boundary of the 22nd group extends only to 2.03 keV, because of the limitation in the number of ultrafine groups permitted by MC<sup>2</sup>. The cutoff at this energy does not induce any significant error in the calculated flux or in the eigenvalue for the present loadings of EBR-II. The set was produced by MC<sup>2</sup> using the current version of the ENDF/B library

TABLE IX. Group Structure of Cross-section Set JM31F

Energy Group	Lower Energy Limit, eV	Upper Lethargy Limit	Corresponding Group		Energy Group	Lower Energy Limit, eV	Upper Lethargy Limit	Corresponding Group		
			Set 238	Set 23806				Set 238	Set 23806	
1	$8.82 \times 10^6$	0.125	1	1	13	$1.97 \times 10^6$	1.625	3	2	
2	$7.79 \times 10^6$	0.250			14	$1.74 \times 10^6$	1.750			
3	$6.87 \times 10^6$	0.375			15	$1.53 \times 10^6$	1.875			
4	$6.07 \times 10^6$	0.500			16	$1.35 \times 10^6$	2.000	4		
5	$5.35 \times 10^6$	0.625			17	$8.21 \times 10^5$	2.500			4
6	$4.72 \times 10^6$	0.750			18	$4.89 \times 10^5$	3.000	5	3	
7	$4.17 \times 10^6$	0.875			19	$3.02 \times 10^5$	3.500	6		
8	$3.68 \times 10^6$	1.000			20	$1.11 \times 10^5$	4.500	7, 8	4	
9	$3.25 \times 10^6$	1.125			21	$4.09 \times 10^4$	5.500	9, 10	5	
10	$2.87 \times 10^6$	1.250	2	2	22	$2.03 \times 10^3$	8.500	11-16	6 <sup>a</sup>	
11	$2.53 \times 10^6$	1.375								
12	$2.23 \times 10^6$	1.500								

<sup>a</sup>Lower energy of group 6 is 29.0 eV.

tape.<sup>15</sup> The compositions of the run-31F loading used to generate the weighting spectra are given in Table X. A buckling search for the core cross section and a buckling value equal to zero were assumed in producing the cross sections for the blanket and reflector regions.

TABLE X. Atomic Densities of Nuclides Used in Generating the Weighting Spectra of Set JM31F

Nuclide	Core	Reflector	Blanket
<sup>235</sup> U	$5.6854 \times 10^{-3}$	-	$6.144 \times 10^{-5}$
<sup>239</sup> Pu	$7.6822 \times 10^{-5}$	-	$1.00 \times 10^{-6}$
<sup>238</sup> U	$4.8993 \times 10^{-3}$	-	$2.78646 \times 10^{-2}$
Fe	$1.2208 \times 10^{-2}$	$3.001 \times 10^{-2}$	$1.17639 \times 10^{-2}$
Ni	$1.59899 \times 10^{-3}$	$3.7995 \times 10^{-3}$	$1.4894 \times 10^{-3}$
Cr	$2.69618 \times 10^{-3}$	$8.5755 \times 10^{-3}$	$3.3616 \times 10^{-3}$
Na	$9.60816 \times 10^{-3}$	$1.12918 \times 10^{-2}$	$4.60703 \times 10^{-3}$
O	$4.56403 \times 10^{-4}$	-	-
C	$1.33004 \times 10^{-4}$	-	-

The ENDF/B data contains cross sections for (n,2n), (n,p), and (n, $\alpha$ ) reactions. Precautions were taken in converting the (n,2n) cross sections to preserve the neutron balance in the neutronic codes. The unusual energy-group structure requires that the full 22-group down-scattering matrix from MC<sup>2</sup> be converted to other formats; the usual practice is to limit the number of down-scatter groups to 12 or 15. The output of the MC<sup>2</sup> problem was converted first to XLIBIT format and then to the formats for the DOT code<sup>16</sup> and the ARC system.<sup>17</sup> Table XI describes set JM31F for both formats.

TABLE XI. Description of Cross-section Set JM31F

Nuclide	Weighting Spectrum	Designation	Nuclide	Weighting Spectrum	Designation
Carbon	C <sup>a</sup>	CAR--C	<sup>238</sup> U	C	U238-C
	B <sup>b</sup>			B	U238-B
	R <sup>c</sup>			R	U238-R
Sodium	C	NA---C	<sup>239</sup> Pu	C	Pu239C
	B	NA---B		B	Pu239B
	R	NA---R		R	Pu239R
<sup>235</sup> U	C	U235-C	Chromium	C	CR---C
	B	U235-B		B	CR---B
	R	U235-R		R	CR---R
Oxygen	C	OXY--C	Nickel	C	NI---C
	B			B	NI---B
	R			R	NI---R
Iron	C	FE---C			
	B	FE---B			
	R	FE---R			

<sup>a</sup>Core.

<sup>b</sup>Reflector.

<sup>c</sup>Blanket.

## B. Comparison of the Neutron Cross-section Sets

One-dimensional neutronic calculations were performed after the input specifications of EBR-II had been prepared and the neutron cross-section sets had been developed. A primary objective of these neutronic calculations was to compare the results obtained by using the various cross-section sets and the neutronic codes.

One-dimensional calculations, discussed in this section, are relatively easy to prepare and use little computer time. Thus, calculations using the 22-energy group sets and high-order transport approximation can be performed economically.

Discrepancies in the early calculation of EBR-II criticality led to investigations that narrowed the sources of the discrepancies to the cross sections and the neutronic model.<sup>18</sup> A series of one-dimensional calculations of a simplified model of EBR-II determined the contribution of each source. Table XII gives the compositions of a three-region spherical model of EBR-II, in which the core (25.2-cm radius) is surrounded by a 10-cm-thick steel reflector and finally by a 35-cm-thick depleted-uranium blanket. The investigation of neutronic codes presented here centers around a comparison of the eigenvalues obtained from diffusion theory and from various orders of the transport approximation<sup>19</sup> for the different cross-section sets. A more complete investigation of a one-dimensional representation of EBR-II will be given in Section IV below.

TABLE XII. Composition of Simplified (Three-region, Spherical Geometry) Model of EBR-II

Nuclide	Concentration, $10^{24}$ atoms/cm <sup>3</sup>		
	25.2-cm-radius Core	10.0-cm-thick Reflector	35-cm-thick Blanket
<sup>235</sup> U	$6.3 \times 10^{-3}$	-	$6.0 \times 10^{-5}$
<sup>238</sup> U	$6.0 \times 10^{-3}$	-	$2.9 \times 10^{-2}$
<sup>239</sup> Pu	$1.0 \times 10^{-5}$	-	$3.0 \times 10^{-5}$
Fe	$1.2 \times 10^{-2}$	$4.5 \times 10^{-2}$	$1.2 \times 10^{-2}$
Ni	$1.5 \times 10^{-3}$	$6.1 \times 10^{-3}$	$1.5 \times 10^{-3}$
Cr	$3.0 \times 10^{-3}$	$1.4 \times 10^{-2}$	$3.0 \times 10^{-3}$
Na	$1.1 \times 10^{-2}$	$4.0 \times 10^{-3}$	$4.0 \times 10^{-3}$
Fission product	$1.0 \times 10^{-4}$	-	-
Mo	$7.0 \times 10^{-4}$	-	-
Nb	$3.0 \times 10^{-6}$	-	-
Zr	$6.0 \times 10^{-4}$	-	-

The critical dimensions were given by a transport calculation using an  $S_n$  order equal to eight and cross-section set 238. Table XIII gives the eigenvalues of the system obtained from various neutronic models and cross-section sets. An eigenvalue of 1.00 was assumed to represent the true value for the purposes of this discussion. The following conclusions can be drawn from the data in Table XIII:

1. Diffusion theory predicts a  $k_{\text{eff}}$  of about  $2\frac{1}{2}\%$  lower than the  $S_8$  value; the  $S_2$  approximation yields a  $k_{\text{eff}}$  of about  $2\frac{1}{2}\%$  higher than the  $S_8$  value. These corrections should be applied to the appropriate neutronic model in spherical geometry. The order of the corrections between the neutronic codes is the same for cylindrical geometry, but the magnitude is reduced.

2. The selection of a weighting spectrum in the reflector region has a significant effect on the value of  $k_{\text{eff}}$ . This effect can be seen by comparing the values of  $k_{\text{eff}}$  for all neutronic representations for Cases 1 and 2 and for Cases 5 and 6 of Table XIII. The only difference between these pairs of cases is the weighting spectrum used for the cross sections of the nuclides in the reflector regions. The use of a spectrum characteristic of reflector material produces a value of  $k_{\text{eff}}$  about 1% less than that produced by blanket-weighted cross sections. The importance of the weighting spectrum was the principal reason for developing sets 238 and 23806.

3. There appears to be little difference in the use of core- or blanket-weighted cross sections in the reflector region. This can be seen in Table XIII by comparing Case 3 with Case 4 and Case 7 with Case 8.

4. The improved treatment of inelastic scattering, incorporated within the latest MC<sup>2</sup> code, appears to have had little effect on the  $k_{\text{eff}}$  value for these cases. The basis for this conclusion can be seen by

TABLE XIII. Values of  $k_{\text{eff}}$  of Spherical Representation of EBR-II for Various Cross-section Sets, Weighting Spectra, and Neutronic Models

Case	Cross-section Set	Weighting Spectrum for Cross Sections in Reflector Region	Diffusion	$S_2$	$S_4$	$S_8$
1	238	Reflector	0.9747	1.0231	1.0019	1.0000
2	238	Blanket	0.9848	1.0331	1.0122	1.0102
3	236	Blanket	0.9858	1.0276	1.0069	1.0050
4	236	Core	0.9855	1.0274	1.0066	1.0047
5	23806	Reflector	0.9758	1.0250	1.0035	1.0016
6	23806	Blanket	0.9866	1.0351	1.0138	1.0119
7	23606	Blanket	0.9894	1.0374	1.0164	1.0144
8	23606	Core	0.9886	1.0367	1.0155	1.0135

comparing Case 2 with Case 3 and Case 6 with Case 7. In all these cases, the identical weighting spectra for the cross section were used in each region, so that the only difference among these cases is in the MC<sup>2</sup> code treatment of inelastic scattering. Set 23605 was not included in this comparison, because a five-group structure was not considered accurate enough for EBR-II analysis, and set JM31F had not yet been developed at the time this analysis took place.

### C. Analysis of the Weighting Spectrum

The weighting spectrum used to generate the broad-group cross sections has a significant effect on the values of the cross sections and on the results of neutronic calculations using the cross sections. This effect was noted in Section B.2 (p. 31), where it was shown that the selection of the weighting spectrum influenced the eigenvalue by ~1%.

A perturbation analysis was conducted to determine the cause of the difference in the  $k_{\text{eff}}$  calculated with cross sections produced from different weighting spectra in the reflector region. The reactivity effects produced by exchanging blanket-weighted and reflector-weighted cross sections in the reflector region were calculated for the individual and total components of  $\Delta k/k$ . The results of the calculations given in Table XIV revealed that the

TABLE XIV. Component and Total Values of  $\Delta k/k$  for the Exchange of Reflector- and Blanket-weighted Cross Sections in the Reflector Region

Nuclide	Capture	Radial Leakage	Elastic Scattering	Inelastic Scattering	Total $\Delta k/k$
<u>Substituting Blanket for Reflector-weighted Cross Sections</u> <u>in Case-1 MACH Calculation</u>					
Fe	$-3.19 \times 10^{-4}$	$8.37 \times 10^{-3}$	$1.44 \times 10^{-4}$	$-1.61 \times 10^{-6}$	$8.20 \times 10^{-3}$
Ni	$-2.61 \times 10^{-5}$	$-4.20 \times 10^{-6}$	$-5.09 \times 10^{-5}$	$-8.70 \times 10^{-7}$	$-8.21 \times 10^{-5}$
Cr	$5.48 \times 10^{-6}$	$1.19 \times 10^{-3}$	$3.14 \times 10^{-5}$	$-2.77 \times 10^{-6}$	$1.23 \times 10^{-3}$
Na	$3.25 \times 10^{-6}$	$5.85 \times 10^{-5}$	$8.00 \times 10^{-6}$	$2.59 \times 10^{-7}$	$7.00 \times 10^{-5}$
Total for mixture	$-3.36 \times 10^{-4}$	$9.62 \times 10^{-3}$	$1.32 \times 10^{-4}$	$-4.99 \times 10^{-6}$	$9.41 \times 10^{-3}$
<u>Substituting Reflector for Blanket-weighted Cross Sections</u> <u>in Case-2 MACH Calculation</u>					
Fe	$2.24 \times 10^{-4}$	$-1.00 \times 10^2$	$-2.36 \times 10^{-4}$	$6.70 \times 10^{-7}$	$-1.00 \times 10^{-2}$
Ni	$2.84 \times 10^{-5}$	$-1.11 \times 10^{-5}$	$2.98 \times 10^{-5}$	$7.87 \times 10^{-7}$	$4.79 \times 10^{-5}$
Cr	$-6.69 \times 10^{-6}$	$-1.18 \times 10^{-3}$	$-3.32 \times 10^{-5}$	$2.19 \times 10^{-6}$	$-1.22 \times 10^{-3}$
Na	$-3.08 \times 10^{-6}$	$-5.06 \times 10^{-5}$	$-1.06 \times 10^{-5}$	$-3.32 \times 10^{-7}$	$-6.46 \times 10^{-5}$
Total for mixture	$2.43 \times 10^{-4}$	$-1.13 \times 10^{-2}$	$-2.50 \times 10^{-4}$	$-3.32 \times 10^{-6}$	$-1.13 \times 10^{-2}$



leakage component contributes most to the reactivity. The exchange of reflector- and blanket-weighted cross sections for iron accounts for 89% of the total difference in the leakage. The values of reactivity for the two substitutions have different absolute values, because of the first-order nature of the perturbation analysis. The sensitivity of the leakage component is related to the discrepancies in the transport cross section. For example, the transport cross section of iron is very sensitive to the weighting spectrum in those energy regions containing large resonance. An 80% difference in the 11th broad-group transport cross section of iron is seen between the cross sections weighted with a reflector spectrum and those weighted with a blanket spectrum.

When the broad-group transport cross sections are generated, the MC<sup>2</sup> code weights the ultrafine-group cross-section data with the ultrafine-group flux and the inverse of the homogenized transport cross section. If the weighting spectrum does not take into account the depressed flux and large homogenized transport cross section in a resonance region, the broad-group cross section will be in error.

Discrepancies in the transport cross sections in resonance regions of iron are expected, because the spectrum characteristic of the blanket does not represent the spectrum in a region of high-iron content. However, the sensitivity of the reactivity to the changes in the cross sections was not expected because: (1) The iron resonances occur at the end of the EBR-II spectrum; (2) the reflector region is thin and is not a region of considerable neutronic worth; and (3) to be significant, all errors must be in the same direction. An investigation showed that the effect of weighting spectrum is important in this case, because even though the real and adjoint fluxes are not large, the gradients of the real and adjoint fluxes in the resonance regions are large as is evident in the following equation:

$$\delta k = \sum_j \delta k_j = \sum_j \nabla \phi_j \cdot \nabla \phi_j^+ \delta \left( \frac{1}{3\Sigma_{tr,j}} \right), \quad (4)$$

where  $j$  = energy group.

Furthermore, the values of the  $\delta k_j$ 's have the same sign for all energies where the perturbation in the transport cross section is large. Some other cross sections were more sensitive to the weighting spectrum than was the transport cross section of iron; however, because of cancelation of errors, these other cross sections had a smaller effect on the reactivity.

When multiregion reactors are analyzed, the choice of the weighting spectrum must be considered, even for small regions of relatively low importance. Three conditions under which the reactivity should be sensitive to the weighting spectrum of the cross section are: (1) when an abundant nuclide has a nuclear property that varies significantly with



energy (usually these are resonances); (2) when that nuclide occurs in substantially different amounts in the reactor than it did in the composition from which the weighting spectrum was generated; and (3) when the nuclear property contributes significantly to the reactivity of the reactor in the energy regions where the variations exist.

#### IV. INVESTIGATION OF ONE-DIMENSIONAL REPRESENTATION OF EBR-II

The investigation of a one-dimensional representation of EBR-II is presented in two sections; Section A compares various neutronic models (diffusion and transport theory); Section B considers the effect of the various geometrical representations of EBR-II on the calculated values of the neutronic parameters.

##### A. Comparison of Results from Diffusion and Transport Calculations

The investigation of the various neutronic models was based on a series of calculations described in Section III.A.6 of this report. In these calculations, EBR-II was represented as a three-region sphere for which diffusion and transport calculations were performed with set 238 (see Case 1, Table XIII). The diffusion theory predicts the lowest eigenvalue, and the  $S_2$  transport approximation yields the highest. The higher-order approximations of transport calculations predict successively lower eigenvalues. As will be seen in the discussion of two-dimensional ( $r, z$ ) results (Section V), the range of eigenvalues from diffusion and transport calculations is found to be smaller in cylindrical geometry than in spherical geometry.

The values of the flux at the core center and at the core-reflector interface are presented in Table XV from the results of the diffusion,  $S_2$ , and  $S_4$  transport calculations. The flux is normalized to one fission neutron/sec for a just-critical system. The fluxes from transport calculation are determined at a point midway between mesh points, and thus the values in Table XV have been interpolated to the core-center and core-edge

TABLE XV.. Flux at Core Center and Edge from  
Diffusion and  $S_2$  and  $S_4$  Transport Calculations

	Flux, $10^{-4}$ n/cm <sup>2</sup> /sec		
	Diffusion	Transport	
		$S_2$	$S_4$
Center	7.679	7.850	7.844
Edge	4.052	4.137	4.099

locations. The flux from the  $S_2$  calculation is higher than that from the other two codes at both the core center and the core edge. Although the values are not presented here, the  $S_2$  transport code yields lower fluxes in the blanket region than do those from the other two cases.

Considering the difference in positions at which the fluxes are given, the fluxes from the  $S_4$  calculation are slightly higher in the core region than are those from diffusion theory.

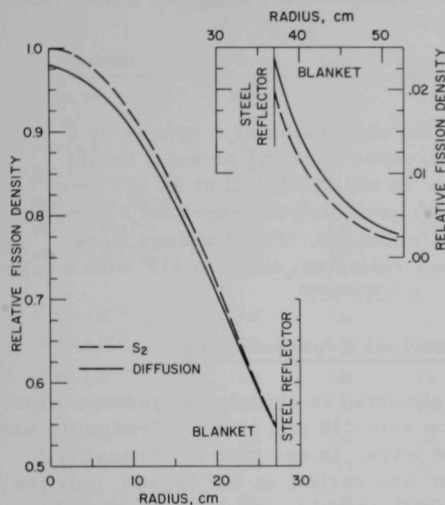


Fig. 11. Fission-density Distribution from  $S_2$  Transport and Diffusion Calculations

The comparison of the relative fission density, as given in Fig. 11, produces the same relationship among the fission densities of the  $S_2$  and diffusion calculations as for the fluxes. Table XVI gives the energy spectra of the flux at the core center and core edge for the three cases. The results are in excellent agreement and differ by only a few percent for any energy group.

Although the selection of the neutronic code can have a 2-3%

TABLE XVI. Fraction of Flux at Core Center and Edge per Group from Diffusion Calculations and  $S_2$  and  $S_4$  Transport Calculations

Group No.	Diffusion		Transport			
	Center	Core Edge	$S_2$		$S_4$	
	Center	Core Edge	Center	Core Edge	Center	Core Edge
1	3.07	1.85	3.19	2.15	3.09	2.10
2	6.00	3.89	5.81	4.06	5.66	3.97
3	9.82	7.01	9.64	7.17	9.43	7.08
4	12.66	9.97	12.75	10.22	12.53	10.19
5	15.80	13.90	16.00	14.06	15.82	14.08
6	16.97	16.17	17.33	16.29	17.19	16.36
7	13.38	14.22	13.68	14.19	13.61	14.25
8	9.74	11.03	9.96	10.96	9.91	11.01
9	5.87	7.49	5.99	7.36	5.96	7.39
10	3.41	5.41	3.47	5.22	3.46	5.24
11	1.68	3.01	1.71	2.89	1.70	2.89
12	1.01	2.77	1.03	2.59	1.01	2.59
13	0.36	1.23	0.37	1.14	0.36	1.14
14	0.15	0.70	0.15	0.64	0.14	0.63
15	0.02	0.21	0.02	0.17	0.02	0.17
16	0.02	0.26	0.02	0.23	0.02	0.23
17	0.02	0.39	0.02	0.35	0.02	0.35
18	-	0.10	-	0.09	-	0.09
19	-	0.12	-	0.11	-	0.11
20	-	0.09	-	0.08	-	0.08
21	-	0.06	-	0.05	-	0.05
22	-	0.05	-	0.02	-	0.02

influence on the eigenvalue and on the magnitude of flux and flux-related quantities, such as power density and reaction rates, it has no substantial effect on the spectrum in the core region. A 2-3% variation, although significant for criticality studies, is acceptable when using the power density in scoping studies.

## B. Effect of Geometrical Approximations

EBR-II may be represented in one dimension as a sphere or a cylinder with an input value of the transverse buckling or axial height. A series of calculations was performed in which EBR-II at 50 MWt was represented in spherical and cylindrical geometry for six- (set 23806) and 22- (set 238) group diffusion-theory calculations. Two loadings were investigated: run 27A with a steel inner reflector, and run 31F with a full depleted-uranium blanket.

### 1. Calculations Using a Cylindrical Representation

Nuclear quantities were calculated in cylindrical geometry for the two loadings and with cross-section sets 238 and 23806. Criticality was achieved for each case in two different ways. In one type of criticality search, the height of the entire reactor was varied; in the second, only the height of the core was varied with the reflector/blanket height remaining

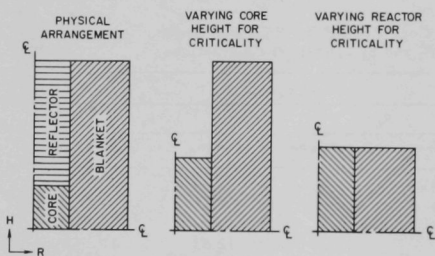


Fig. 12. Pictorial Representation of Two Approaches to Calculating Criticality in One-dimensional Cylindrical Geometry

at 139.5 cm. Figure 12 shows these two models. The height of 139.5 cm is the physical height of the depleted-uranium slugs in the blanket sub-assemblies. Neither model represents the axial direction correctly, as will be seen in Section V. However, the results from the two approaches provide a means of investigating the effect of approximating the axial direction in one-dimensional calculations. Table XVII gives the results of the diffusion calculations for eight cases.

The critical heights of the core for run 27A, obtained from the two approaches to criticality, differ by over 5 cm. For run 31F, however, the difference is only slightly over 2 cm. The presence of a steel reflector makes a one-dimensional representation more difficult to obtain than it is for loadings with a full depleted-uranium blanket; this will be discussed more thoroughly in Section V.K.

TABLE XVII. Results from the Eight Cases Using One-dimensional, Cylindrical Representations of EBR-II at 50 MWt

Quantities	Case 1	Case 2	Case 3	Case 4	Case 5	Case 6	Case 7	Case 8
	Run 27A				Run 31F			
	Set 238		Set 23806		Set 238		Set 23806	
	Uniform <sup>a</sup>	Core <sup>a</sup>	Uniform <sup>a</sup>	Core <sup>a</sup>	Uniform <sup>a</sup>	Core <sup>a</sup>	Uniform <sup>a</sup>	Core <sup>a</sup>
Height, cm	66.935	61.561	66.936	61.578	64.287	60.960	64.265	60.972
$\beta \times 10^3$	6.91	6.93	6.92	6.94	7.01	7.24	6.99	7.21
$k(\text{sec}) \times 10^7$	1.02	1.66	1.05	1.66	0.810	1.03	0.866	1.11
$1h/\% \Delta k$	433	436	434	435	437	437	437	436
Max/avg power density	1.67	1.57	1.67	1.58	1.59	1.53	1.59	1.54
$\rho(0), 10^{13} \text{ f/cm}^3/\text{sec}$	2.65	2.49	2.65	2.49	2.40	2.30	2.42	2.32
$\rho(R), 10^{13} \text{ f/cm}^3/\text{sec}$	1.30	1.42	1.27	1.38	1.23	1.29	1.24	1.30
Reactions/sec at Core Center (O) and Core Edge (R)								
$\sigma_f^{25}\rho(O) \times 10^{-15}$	3.52	3.31	3.53	3.31	3.24	3.11	3.27	3.13
$\sigma_f^{25}\rho(R) \times 10^{-15}$	2.06	2.26	2.02	2.20	1.84	1.93	1.85	1.94
$\sigma_f^{49}\rho(O) \times 10^{-15}$	4.26	4.00	4.25	3.99	3.89	3.73	3.92	3.76
$\sigma_f^{49}\rho(R) \times 10^{-15}$	2.29	2.48	2.26	2.43	2.11	2.20	2.11	2.20
$\sigma_f^{28}\rho(O) \times 10^{-14}$	2.46	2.31	2.45	2.31	2.10	2.01	2.09	2.00
$\sigma_f^{28}\rho(R) \times 10^{-14}$	0.96	0.98	0.97	1.00	0.89	0.90	0.91	0.93
$\sigma_f^{28}\rho(O)/\sigma_f^{25}\rho(O) \times 10^{-2}$	6.82	6.98	6.96	6.95	6.48	6.48	6.39	6.38
$\sigma_f^{28}\rho(R)/\sigma_f^{25}\rho(R) \times 10^{-2}$	4.64	4.34	4.82	4.54	4.82	4.66	4.94	4.79
Nuclide Worth ( $\Delta k/k/V$ ) for $1.0\text{-g/cm}^3$ Increase at Core Center, Whole Core and Inner Blanket								
$^{235}\text{U}$ center $\times 10^6$	3.34	3.17	3.34	3.17	3.12	2.86	3.25	2.99
$^{235}\text{U}$ core $\times 10^6$	2.06	2.11	2.06	2.12	2.01	1.94	2.03	1.97
$^{235}\text{U}$ inner blanket $\times 10^6$	0.82	0.68	0.80	0.65	0.82	0.60	0.81	0.59
$^{239}\text{Pu}$ center $\times 10^6$	5.77	5.44	5.75	5.43	5.36	4.88	5.54	5.08
$^{239}\text{Pu}$ core $\times 10^6$	3.46	3.54	3.45	3.54	3.38	3.26	3.40	3.30
$^{239}\text{Pu}$ inner blanket $\times 10^6$	1.22	1.00	1.20	0.98	1.23	0.89	1.20	0.87
$^{238}\text{U}$ center $\times 10^7$	1.30	1.44	1.35	1.49	1.06	1.10	1.00	1.06
$^{238}\text{U}$ core $\times 10^7$	1.28	1.18	1.31	1.23	1.17	1.05	1.20	1.10
$^{238}\text{U}$ inner blanket $\times 10^8$	5.61	1.48	6.22	2.10	4.98	1.78	5.46	2.18
Fe center $\times 10^7$	0.86	1.17	0.81	1.12	0.97	1.10	0.73	0.91
Fe core $\times 10^7$	1.58	1.51	1.55	1.50	1.39	1.26	1.39	1.27
Fe inner blanket $\times 10^7$	1.39	0.72	1.40	0.74	1.09	0.52	1.13	0.56
Na center $\times 10^7$	6.63	7.08	6.18	6.67	6.66	6.59	5.91	5.99
Na core $\times 10^7$	6.33	6.18	6.07	5.94	5.88	5.42	5.63	5.22
Na inner blanket $\times 10^7$	4.06	2.24	4.01	2.22	3.17	1.54	3.10	1.53

<sup>a</sup>Criticality searches (see Fig. 12). Uniform: reactor height varied uniformly to achieve criticality. Core: only core height varied to achieve criticality.

Selection of an axial representation significantly influences some nuclear quantities. This influence can be traced to a larger transverse (axial) leakage from the core as predicted in those cases where only the core height was varied for criticality (Cases 2, 4, 6, and 8 of Table XVII). The affected nuclear parameters include the prompt-neutron lifetime, the power density, the various reaction rates, and the materials worths in the core center, the whole core, and the inner blanket. The difference in these nuclear parameters due to the different axial representation is also greater for run 27A with a steel reflector than for run 31F.

The results obtained from sets 238 and 23806 are in good agreement. The largest discrepancies between six- and 22-group results are seen in the worth of  $^{238}\text{U}$  in the inner blanket. The fission cross section of  $^{238}\text{U}$  cannot be represented adequately by the six-group structure in the regions where the fast-flux spectrum changes significantly as a function of position, such as in the inner blanket. Except for  $^{238}\text{U}$  fission rates and material worth in the outer core or blanket regions, the agreement between the quantities obtained from six- and 22-group calculations is better than 5%.

Table XVIII gives the values of fission density on the radial midplane line at the inner and outer radii of the first eight rows and at

TABLE XVIII. Fission Densities at 50 MWt  
by Row from One-dimensional, Cylindrical  
Calculations of Runs 27A and 31F

Row	Position	Fission Densities, $10^{13} \text{ f/cm}^3/\text{sec}$			
		Run 27A		Run 31F	
		Uniform	Core	Uniform	Core
1	Inner	2.96	2.84	2.71	2.63
	Outer	2.94	2.82	2.68	2.61
2	Inner	1.73	1.66	1.34	1.30
	Outer	1.67	1.62	1.30	1.27
3	Inner	2.55	2.47	2.29	2.23
	Outer	2.37	2.32	2.14	2.21
4	Inner	1.80	1.76	1.90	1.87
	Outer	1.61	1.61	1.70	1.70
5	Inner	1.82	1.82	1.72	1.72
	Outer	1.56	1.63	1.49	1.52
6	Inner	1.74	1.81	1.73	1.76
	Outer	1.45	1.62	1.39	1.48
7	Inner			0.290	0.299
	Outer			0.106	0.114
8	Inner			0.106	0.114
	Outer			0.0410	0.0457
9	Inner	0.0546	0.0559	0.0410	0.0457
10	Radius = 50 cm	0.0119	0.0132	0.0090	0.0100

two additional locations in the outer blanket for Cases 1, 2, 5, and 6 of Table XVII. Table XIX presents the regional power fraction for these four cases. The values of the power fission density and power fraction from the six-group calculations were not included, because they differ only slightly from the 22-group results. The power production is flatter in Cases 2 and 6, where criticality was obtained by varying only the core height. In Section V, the results in Tables XVIII and XIX, which are consistent with those discussed earlier in this section, will be compared with the values for two-dimensional calculations.

TABLE XIX. Fraction of Power by Region from One-dimensional, Cylindrical Calculations of Runs 27A and 31F

Region	Run 27A		Run 31F	
	Uniform	Core	Uniform	Core
Row 1	0.0179	0.0168	0.0161	0.0154
Row 2	0.0617	0.0582	0.0471	0.0452
Row 3	0.1793	0.1708	0.1590	0.1538
Row 4	0.1868	0.1813	0.1939	0.1898
Row 5	0.2454	0.2452	0.2301	0.2292
Row 6	0.2875	0.3024	0.2775	0.2847
Inner blanket	0.0	0.0	0.0604	0.0630
Outer blanket	0.0214	0.0254	0.0160	0.0189

The two approximations of the axial dimension in the cylindrical calculations are based on widely different physical representations of EBR-II. However, the nuclear quantities obtained from these two representations yield results that agree sufficiently for scoping and similar types of studies. Most results agree within 10-20%. An analysis of the two-dimensional representation in Section V will show that the one- and two-dimensional results agree fairly well; this agreement supports the claim that a one-dimensional analysis is useful for studying EBR-II.

## 2. Calculations Using a Spherical Representation

The two EBR-II loadings, runs 27A and 31F, were represented as a three-region sphere in the six- and 22-group diffusion-theory calculations. The six rows of the core were homogenized to one region; the inner and outer blankets comprise the other two regions. The core radius was varied to achieve criticality for the four cases, and Table XX shows the results.

The agreement between the results obtained from the six- and 22-group sets is good, as was the agreement of results of the cylindrical calculations.

TABLE XX. Results from the Four Cases Using One-dimensional, Spherical Representation of EBR-II at 50 MWt

Quantities	Case 1	Case 2	Case 3	Case 4
	Run 27A		Run 31F	
	Set 238	Set 23806	Set 238	Set 23806
Radius, cm	27.365	27.308	28.636	28.731
Volume, liters	85.84	85.30	98.36	99.34
$\beta \times 10^3$	6.84	6.86	7.00	7.05
$l(\text{sec}) \times 10^7$	1.41	1.44	0.89	0.97
$Ih/\% \Delta k$	440	438	454	448
Max/avg Power Density	1.40	1.41	1.27	1.27
$\rho(O), 10^{13} \text{ f/cm}^3/\text{sec}$	2.39	2.41	1.68	1.69
$\rho(R), 10^{13} \text{ f/cm}^3/\text{sec}$	1.38	1.35	1.13	1.14
Reactions/sec at Core Center (O) and Core Edge (R)				
$\sigma_f^{25}\varphi(O) \times 10^{-15}$	4.07	4.11	2.71	2.72
$\sigma_f^{25}\varphi(R) \times 10^{-15}$	2.41	2.36	1.88	1.88
$\sigma_f^{44}\varphi(O) \times 10^{-15}$	4.89	4.92	3.37	3.37
$\sigma_f^{44}\varphi(R) \times 10^{-15}$	2.61	2.57	2.19	2.18
$\sigma_f^{28}\varphi(O) \times 10^{-14}$	2.84	2.84	2.33	2.33
$\sigma_f^{28}\varphi(R) \times 10^{-14}$	1.00	1.02	1.02	1.06
$\sigma_f^{28}\varphi(O)/\sigma_f^{25}\varphi(O) \times 10^{-2}$	6.97	6.91	8.59	8.57
$\sigma_f^{28}\varphi(R)/\sigma_f^{25}\varphi(R) \times 10^{-2}$	4.15	4.34	5.47	5.62
Nuclide Worth ( $\Delta k/k/V$ ) for 1.0-g/cm <sup>3</sup> Increase at Core Center, Whole Core, and Inner Blanket				
<sup>235</sup> U center $\times 10^6$	5.08	5.16	3.26	3.28
<sup>235</sup> U core $\times 10^6$	2.70	2.72	2.19	2.17
<sup>235</sup> U inner blanket $\times 10^6$	1.26	1.21	1.26	1.23
<sup>239</sup> Pu center $\times 10^6$	8.81	8.84	5.74	5.75
<sup>239</sup> Pu core $\times 10^6$	4.46	4.49	3.66	3.63
<sup>239</sup> Pu inner blanket $\times 10^6$	1.82	1.79	1.90	1.86
<sup>238</sup> U center $\times 10^7$	0.89	0.96	0.98	1.14
<sup>238</sup> U core $\times 10^7$	1.29	1.35	1.14	1.30
<sup>238</sup> U inner blanket $\times 10^7$	5.78	6.91	7.49	8.40
Fe center $\times 10^7$	-0.38	-0.44	-0.93	-0.85
Fe core $\times 10^7$	1.91	1.92	1.00	1.12
Fe inner blanket $\times 10^7$	1.80	1.86	1.57	1.66
Na center $\times 10^7$	5.89	5.16	2.81	2.18
Na core $\times 10^7$	7.59	7.32	4.53	4.21
Na inner blanket $\times 10^7$	5.23	5.26	4.51	4.40



Considerable differences exist between the neutronic quantities calculated for run 27A and those for run 31F. The differences arise from the difference in the calculated critical radii for the two loadings of 1.5 cm and therefore in core volumes of over 12 liters. Because both systems are normalized to 50 MWt, the flux and reaction rates in the smaller core (run 27A) are higher than those in the larger core (run 31F). A meaningful comparison of the results of runs 27A and 31F is not possible, because material worths and other nuclear characteristics are greatly influenced by the core size and other directly related quantities.

Some results of calculations of the spherical model differ significantly from those of the cylindrical model, the largest discrepancies occurring in quantities that are sensitive to the geometrical parameters. Neutron lifetime and material worths in which leakage plays an important role are two examples. The lifetimes differ by 50% between the spherical and cylindrical representations; the worth of iron at the core center is negative in the spherical, but positive in the cylindrical, calculations. The difference in the core loadings between the spherical and cylindrical representations influences the material worths and the reaction rates of  $^{235}\text{U}$ ,  $^{238}\text{U}$ , and  $^{239}\text{Pu}$ . The core volume of ~95 liters for both loadings in the cylindrical model falls between the values for the two loadings in the spherical calculation. The reaction rates and material worths of  $^{235}\text{U}$ ,  $^{238}\text{U}$ , and  $^{239}\text{Pu}$  from cylindrical calculations also fall between those from the spherical calculations.

The reaction rates, power density, and material worths have been averaged over the axial dimension in the cylindrical calculations, and therefore they should be compared to the spherical results with this in mind. Because of the sensitivity of many neutronic quantities to the core size, the accuracy of the spherical representation depends on how well the critical core volume has been predicted.

## V. INVESTIGATION OF TWO-DIMENSIONAL REPRESENTATION OF EBR-II

### A. Introduction

A two-dimensional analysis of EBR-II was conducted for runs 27A and 31F to investigate the various neutronic codes and cross-section sets and to compare the results with those from the one-dimensional analysis. EBR-II was represented in (r,z) geometry with 24 material regions and 26 x 46 mesh intervals in the (r,z) directions, respectively. The preparation of the input specifications was discussed in Section II.D; Fig. 13 shows the arrangements of the regions for the two-dimensional calculations. The calculations were carried out with three neutronic codes: SNARG-2D,<sup>13</sup> DOT,<sup>17</sup> and DIF-2D.<sup>18</sup> The SNARG-2D and DOT codes are transport-theory



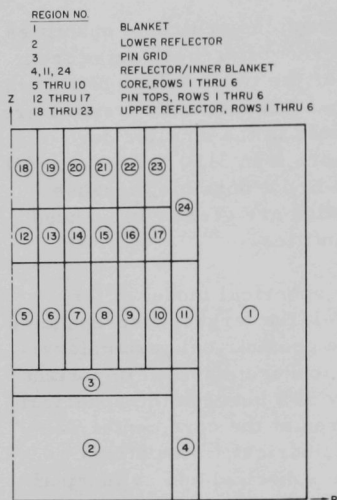


Fig. 13. Representation of EBR-II for Two-dimensional ( $r, z$ ) Calculations with Region Numbers and Identification. ANL Neg. No. 113-1511 Rev. 1.

codes; the DIF-2D is a diffusion-theory code. Cross-section sets 238, 23806, and JM31F were used in the series of eight calculations described in Table XXI. Set JM31F does not contain cross-section data for some nuclides in fission. Moreover, the cross sections for the fission products available in the ENDF/B library were not comparable to those on the old library tape. To enable a comparison of results, no fission or fission products were included in the compositions for these calculations. However, additional calculations were performed using sets 238 and 23806 with fission products and fission to investigate the effect of their absence. Currently the two-dimensional codes do not contain the ancillary routines that the one-dimensional diffusion codes do; thus a full comparison cannot be made among the various neutronic quantities obtained from the one-dimensional calculations in Section IV.

Sections B-K below compare the results from the eight two-dimensional calculations with one another and with the results of the one-dimensional calculations.

TABLE XXI. Description and Partial Results of the Two-dimensional Calculations of EBR-II, Run 31F at 50 MWt

Case No.	Code	Cross-section Set	Fission Product and Fission	$k_{eff}$	Center Flux $\times 10^{-15}$	Fission Ratio
1	SNARC-2D S <sub>2</sub>	23806	No	1.02972	2.657	0.0657
2	DOT S <sub>2</sub>	23806	No	1.02955	2.657	0.0658
3	DOT S <sub>4</sub>	23806	No	1.02209	2.583	0.0659
4	DOT S <sub>2</sub>	238	No	1.02984	2.658	0.0647
5	DOT S <sub>2</sub>	JM31F	No	1.03235	2.744	0.0613
6	DIF-2D	23806	No	0.99851	2.495	0.0650
7	DIF-2D	238	No	1.00006	2.491	0.0639
8	DIF-2D	JM31F	No	1.00208	2.556	0.0607
9	DOT S <sub>2</sub>	238	Yes	1.03131	2.696	0.0633
10	DIF-2D	238	Yes	1.00211	2.526	0.0625

## B. Comparison of Eigenvalues of the Eight Two-dimensional Calculations

Table XXI gives the eigenvalues and the values of the centerline flux and the fission ratio of  $^{238}\text{U}/^{235}\text{U}$  for the eight two-dimensional calculations. All problems were flux-convergence types with a convergence criterion of  $1 \times 10^{-5}$ .

As was seen in the one-dimensional analysis, the transport approximation (Cases 1-5 of Table XXI) yields a higher eigenvalue than do the diffusion calculations (Cases 6-8). The eigenvalue of the  $S_4$  transport calculation falls between the values of the  $S_2$  transport calculation and that of the diffusion theory; the differences in the eigenvalue from the various neutronic approximations are much smaller in two-dimensional (r,z) geometry than in the one-dimensional, spherical model. The difference in eigenvalue between the diffusion theory and the  $S_2$  transport calculations is about 5% for a sphere but only 2% for the two-dimensional, cylindrical model. The very close comparison of the eigenvalue from the SNARG-2D code and the DOT code indicates an identical, or almost identical, formulation of the neutron-transport phenomenon.

The selection of the cross-section sets has a small, but perceptible, effect on the eigenvalue. The values of  $k_{\text{eff}}$  obtained using sets 238 and 23806 are in close agreement; the maximum discrepancy between cases obtained from the same code is 0.1%. Cross-section set JM31F yields a higher value of  $k_{\text{eff}}$  by about 0.2% for both transport and diffusion calculations than those obtained using set 238.

## C. Comparison of Fluxes at the Core Center

The results of the SNARG-2D and DOT codes are normalized to one fission neutron per second in the reactor, and the normalization in the DIF-2D code is one fission per second in the reactor. With a value of 199 MeV per fission, a conversion factor for flux at 50 MWt operation has been calculated to be  $1.567 \times 10^{18}$  for the DIF-2D results. The conversion factor must be multiplied by the average number of neutrons per fission to normalize the results from the SNARG-2D and DOT codes to 50 MWt. The output from these codes does not contain the value for the average number of neutrons per fission. An approximate value was obtained by calculating  $v^{25}$  and  $v^{28}$  along the axial and radial centerlines from the fluxes of the DOT and SNARG calculations. This procedure yielded a value of 2.52 neutrons per fission. The values of the flux were normalized to 50 MWt and then corrected by dividing the normalized flux by the eigenvalue, so that the final value obtained is that for 50-MWt operation of a just-critical reactor.

The values of the flux for the eight cases are in good agreement. The  $S_2$  transport calculation gives the largest values; the diffusion-theory

calculation gives the smallest value of the flux. Cross-section set JM31F produced a noticeably higher value for the flux than that obtained from sets 238 and 23806. Thus, the influence of the neutronic code and of the cross-section sets on the value of the flux at the core center is in the same direction as it was for the eigenvalue.

#### D. Comparison of Fission Ratios

The ratio of fission of  $^{238}\text{U}$  to that of  $^{235}\text{U}$  is a sensitive indicator of the neutron energy spectrum. The values for the fission ratio are influenced by both the high-energy portion in the spectrum and the values of the fission cross sections. Results of set 23806 give the highest value for the fission ratio; those of set JM31F produce the smallest value. Although other factors are important and will be discussed later, the greater the number of energy groups in the high-energy portion of the spectrum, the lower the value of the fission ratio. The fission ratios obtained from the transport calculations are about 1% higher than those obtained from the diffusion calculations for the same cross-section sets; however, this difference produces a small discrepancy for a quantity such as the fission ratio.

#### E. Comparison of Neutron Spectra

##### 1. Comparison of the 22-group Spectra

The addition of both the DIF-2D code in the ARC system and of the DOT code substantially increased the capability of calculating multigroup problems in two dimensions. A 22-group, two-dimensional calculation can be performed in diffusion or  $S_2$  transport theory in less than 1 hr. Of particular interest in performing these calculations is the determination of the spatial effects on the spectrum. Figures 14 and 15 plot the 22-group flux spectra from the DIF-2D and DOT codes, respectively, at five locations in run 31F. The locations are: (1) core center; (2) interface between core and radial blanket; (3) 10 cm into the radial blanket; (4) interface between core and upper axial reflector; and (5) 10 cm into the upper axial reflector.

The spectra within the core (locations 1, 2, and 4) are quite similar for the two calculations. At the core edge, particularly at the interface between the core and the upper axial reflector, there is a slight softening of the spectrum. The spectrum in the radial blanket is noticeably softer than that in the core center; however, little flux exists below the 14th group. The spectrum at this point is approaching that characteristic of a depleted-uranium region. The most substantial change in the spectrum is at location 5. The fraction of the flux at this location in the first six energy groups is reduced compared to that at the core center; an appreciable amount of flux is present to the 22nd group. The structure of the

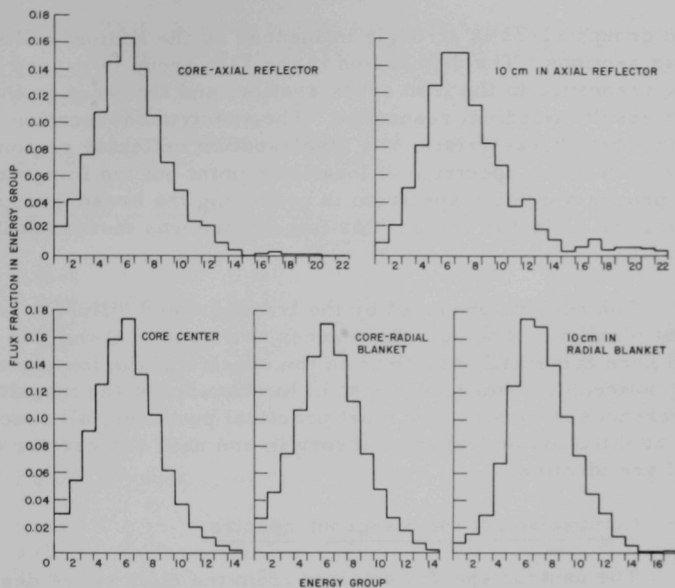


Fig. 14. Flux Spectra of Set 238 at Five Locations in Run 31F,  
Obtained from DIF-2D Calculations

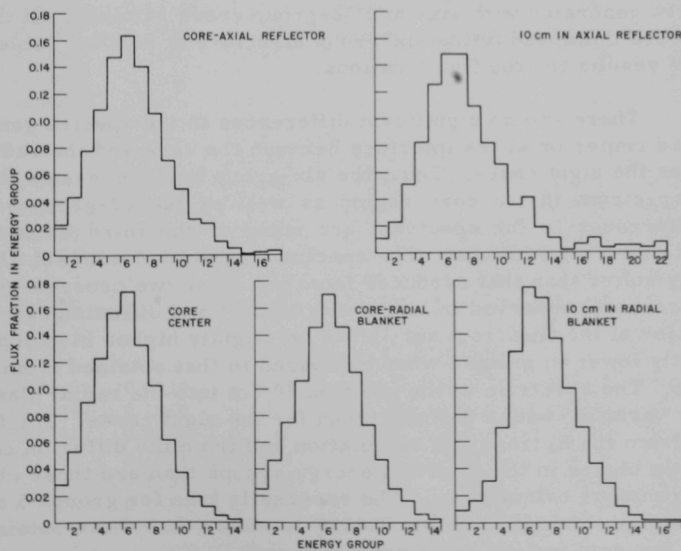


Fig. 15. Flux Spectra of Set 238 at Five Locations in Run 31F,  
Obtained from DOT Calculations ( $S_2$ )

spectra in groups 11-22 is strongly influenced by the sodium and stainless steel cross sections. The depression in the 11th group is caused by the scattering resonance in the iron cross section, and that seen in the 15th group is a result of sodium resonance. The spectrum at location 5 is approaching that characteristic of a steel-sodium reflector region. The variations seen in the spectrum at location 5 point out the importance of using the proper weighting spectrum in producing the broad-group cross sections for the reflector region; this importance was discussed in detail in Section III.C.

The spectra produced by the transport and diffusion calculations are almost identical. The only differences that appear at the five locations presented here are small variations in the spectra of the low-energy range. The most noticeable differences exist in location 5, but the magnitude of these differences is small. For most practical purposes, all spectra produced by diffusion or transport theory in and near the reactor core of EBR-II are identical.

## 2. Comparison of the Six-group Spectra

The neutron spectra obtained from the eight cases described in Table XXI were compared for the five locations in EBR-II. In this study, the location at the core upper-axial reflector interface was replaced by a location 20 cm into the radial blanket. The other four locations are the same as those in the study discussed in Section V.E.1. To compare the spectra generated with six- and 22-group cross sections, all the spectra were collapsed to the six-group structure of 23806. Table XXII shows the results for the five locations.

There are no significant differences in the spectra generated at the core center or at the interface between the core and the radial blanket for the eight cases. Thus, the six-group set represents the EBR-II spectrum in the core region as well as the 22-group set. Some differences in the spectrum are noted at the third location, 10 cm into the radial blanket. The spectrum generated with set JM31F is slightly softer than that produced from the other two cross-section sets; this difference is observed in both the transport and diffusion calculations. The fraction of the flux from set JM31F is slightly higher in groups 5 and 6 and slightly lower in group 2 when compared to that obtained from sets 238 and 23806. The spectrum at the position 20 cm into the radial blanket shows a greater variation with a definite trend for the eight cases. The fluxes obtained from the  $S_4$  transport calculation and from the diffusion calculations are slightly higher in the first two energy groups than are those obtained from  $S_2$  transport calculations. The reverse is true for groups 5 and 6. Again, the flux obtained from set JM31F is softer than those obtained from the other two sets for the same neutronic code.

TABLE XXII. Fraction of Flux per Group at Five Locations for the  
Eight Two-dimensional Calculations of Run 31F

Code:	SNARG	DOT S <sub>2</sub>			DOT S <sub>4</sub>		DIF-2D	
Set:	23808	23806	238	JM31F	23806	23806	238	JM31F
Group								
Core Center								
1	0.0840	0.0840	0.0829	0.0798	0.0845	0.0828	0.0817	0.078
2	0.2196	0.2196	0.2157	0.2086	0.2195	0.2182	0.2145	0.2084
3	0.3306	0.3306	0.3314	0.3394	0.3301	0.3297	0.3305	0.3374
4	0.2340	0.2340	0.2349	0.2374	0.2339	0.2349	0.2358	0.2375
5	0.0955	0.0956	0.0974	0.0970	0.0957	0.0969	0.0986	0.0983
6	0.0363	0.0363	0.0377	0.0378	0.0365	0.0375	0.0389	0.0398
Radial Core Edge								
1	0.0708	0.0708	0.0702	0.0678	0.0726	0.0725	0.0702	0.0691
2	0.1835	0.1835	0.1796	0.1665	0.1862	0.1848	0.1796	0.1677
3	0.3140	0.3141	0.3165	0.3199	0.3140	0.3134	0.3165	0.3190
4	0.2592	0.2591	0.2599	0.2618	0.2571	0.2579	0.2599	0.2601
5	0.1210	0.1210	0.1209	0.1299	0.1195	0.1203	0.1209	0.1277
6	0.0516	0.0516	0.0529	0.0542	0.0507	0.0512	0.0529	0.0563
10 cm into Radial Blanket								
1	0.0219	0.0219	0.0222	0.0204	0.0218	0.0255	0.0222	0.0235
2	0.0976	0.0976	0.0952	0.0727	0.0971	0.1046	0.0952	0.0773
3	0.2950	0.2950	0.3005	0.2882	0.2960	0.2962	0.3005	0.2924
4	0.3090	0.3090	0.3084	0.3083	0.3097	0.3046	0.3084	0.3026
5	0.1782	0.1782	0.1755	0.2074	0.1779	0.1740	0.1755	0.1974
6	0.0983	0.0983	0.0982	0.1031	0.0976	0.0952	0.0982	0.1069
20 cm into Radial Blanket								
1	0.0032	0.0032	0.0029	0.0025	0.0071	0.0066	0.0065	0.0054
2	0.0312	0.0312	0.0303	0.0178	0.0439	0.0440	0.0427	0.0257
3	0.2239	0.2239	0.2223	0.1908	0.2336	0.2368	0.2373	0.2096
4	0.3280	0.3280	0.3283	0.3163	0.3228	0.3235	0.3236	0.3106
5	0.2417	0.2417	0.2416	0.2917	0.2314	0.2301	0.2288	0.2667
6	0.1719	0.1720	0.1746	0.1809	0.1612	0.1590	0.1611	0.1820
10 cm into Axial Reflector								
1	0.0339	0.0339	0.0337	0.0317	0.0279	0.0343	0.0338	0.0264
2	0.1329	0.1329	0.1310	0.1240	0.1241	0.1350	0.1324	0.1162
3	0.2752	0.2752	0.2742	0.2816	0.2747	0.2764	0.2739	0.2630
4	0.2591	0.2591	0.2604	0.2546	0.2640	0.2577	0.2571	0.2504
5	0.1533	0.1533	0.1483	0.1452	0.1582	0.1529	0.1469	0.1512
6	0.1456	0.1456	0.1524	0.1629	0.1511	0.1437	0.1559	0.1928

Recent investigation has revealed that the inelastic removal cross section for  $^{238}\text{U}$  from the ENDF/B library is larger than those from the old MC<sup>2</sup> library.<sup>20</sup> Thus a cross-section set derived from ENDF/B, such as JM31F, would predict greater removal from the higher energies and a correspondingly larger flux at the lower energy. The findings in the radial blanket, which is heavily loaded with  $^{238}\text{U}$ , support this investigation of the inelastic removal cross sections. The larger removal cross section would also explain the low value of the  $^{238}\text{U}/^{235}\text{U}$  fission ratio obtained from calculations using set JM31F.

A discrepancy in the spectra of the eight cases exists in the upper axial reflector, but the trends are not as clear as are those for the spectra deep within the radial blanket. The spectrum generated from set JM31F is softer than those generated from the other cross sections, as was also the case in the radial blanket. The  $S_4$  transport calculation gives a slightly lower fraction of the flux in groups 1 and 2 and a higher fraction in group 4 than the fraction of the flux obtained from diffusion or  $S_2$  transport calculations.

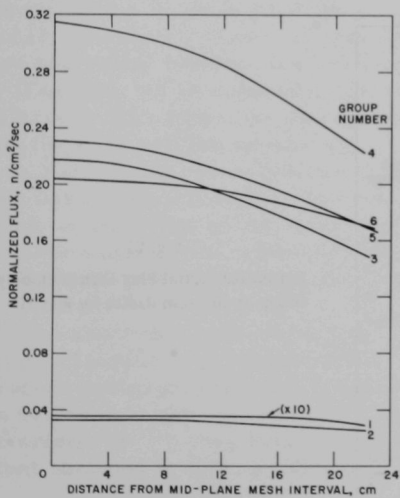
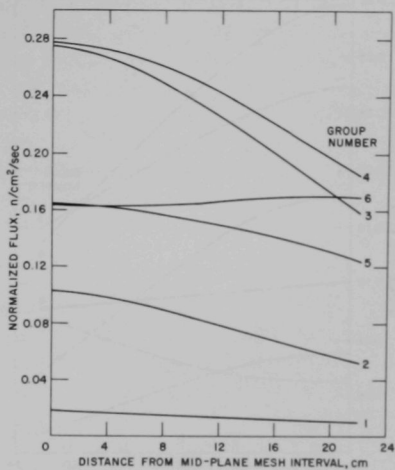
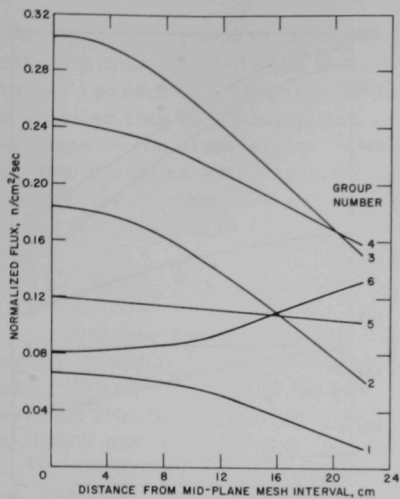
#### F. Nonseparability of the Radial and Axial Fluxes

As was discussed in Section IV, the radial and axial fluxes cannot be separated. To demonstrate this, the axial distributions of the group fluxes from cross-section set 23806 were plotted at three radial positions in EBR-II, runs 27A and 31F. The radial positions are 28.4 cm (row 6), 36.5 cm (row 8), and 50.0 cm (row 10) from the core centerline. The flux distributions, normalized to a value of 1.0 at the radial centerline for each radial position and for each core loading, are shown in Figs. 16-21.

Both the spectrum and distribution of the axial flux change with radial position. A comparison of the plots for runs 27A and 31F reveals that the relative flux in the first two groups decreases, but that in the last two groups increases, with radial position. The relative magnitude of the third- and fourth-group fluxes remains about the same at the three positions. Thus the spectrum becomes softer as the distance from the core center increases. The changes in the axial flux distribution consist of: (a) a flatter distribution with increasing radial distance in groups 1 and 2, (b) little change in the shape of the third- and fourth-group fluxes, and (c) a more convex shape in the fifth- and sixth-group fluxes. The shape of the flux distribution for the sixth group is concave in row 6, flat in row 8, and convex in row 10. Therefore, the axial buckling is both energy and spatially dependent.

The presence of the steel in rows 7 and 8 affects the axial flux spectrum and distribution, as can be seen by comparing the results from runs 27A and 31F. At 28.4 cm, the flux distributions for all energy groups are about the same for both loadings at this position, although the sixth-group flux is greater for run 27A than for run 31F. The largest differences







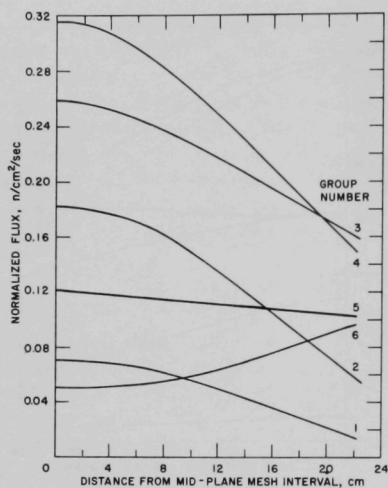


Fig. 19. Normalized Axial Flux Distribution by Group at 28.4-cm Radius for Run 31F

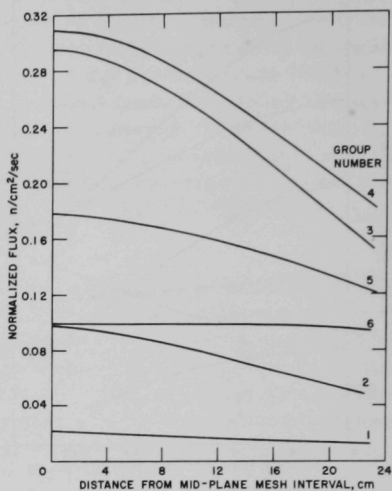


Fig. 20. Normalized Axial Flux Distribution by Group at 36.5-cm Radius for Run 31F

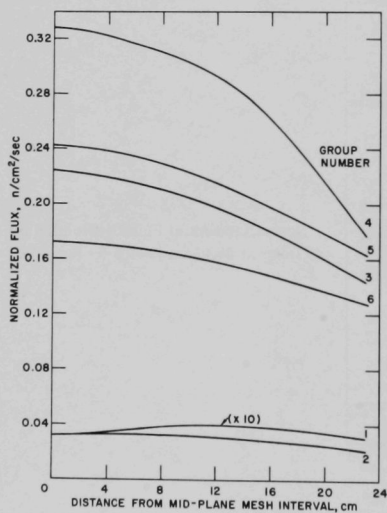


Fig. 21  
Normalized Axial Flux Distribution by Group at 50.0-cm Radius for Run 31F

in the fluxes are found in the inner-blanket/reflector region, where a difference in material between the two loadings occurs. Depleted uranium (run 31F) produced a larger relative flux in the third and fourth groups and smaller flux in the sixth group, as compared to the fluxes from run 27A. The shape of the sixth-group flux distribution is concave with steel in the region, but convex with depleted uranium. In the outer-blanket region (row 10), the flux spectra and distributions are similar for each loading; the flux for run 27A is slightly softer and flatter than that for run 31F.

### G. High-energy Reactions in EBR-II

A major purpose for developing cross-section set JM31F was to investigate some of the dosimetry measurements made in the run 31F loading of EBR-II. The dosimetry experiments included materials with threshold reactions such as (n,p) and (n, $\alpha$ ). The results obtained from set JM31F and presented in this section consider only the high-energy (>1.35 MeV) portion of the spectrum. Table XXII compares set JM31F with the other cross-section sets over the full energy range.

The high-energy parts of the spectra (groups 1-16) at various positions in EBR-II, run 31F, are shown in Figs. 22-26. In this portion of the spectrum, high resolution has been unobtainable from previous cross-section sets. Totaling the flux in the first 16 groups of the five locations yields a value in good agreement with that previously calculated by set 238. Figure 23 shows that the spectrum, at the interface between the core and radial blanket, has the same shape as that in the reactor center (Fig. 22), but is reduced by an almost constant amount in each energy group. The same has been found for the spectrum at the interface between the core and the upper-reflector region (Fig. 24). However, as shown in Fig. 25, the investigation of the spectrum in the region above the core has shown a change in the shape as well as a decrease in the magnitude of total flux in the 16 groups. Although the shape of the spectrum remains the same in the radial blanket as it is in the core center, Fig. 26 shows that it is reduced by a nearly constant amount in each energy group.

The neutronic code requires all fission neutrons to have the same spectrum, regardless of whether  $^{235}\text{U}$ ,  $^{238}\text{U}$ , or  $^{239}\text{Pu}$  is the fissioned isotope. The neutron spectrum from the fissioning of  $^{235}\text{U}$  was used to represent all fission neutrons in the calculations. The use of a neutron fission spectrum characteristic of  $^{238}\text{U}$  may produce a flux spectrum in the blanket different from that obtained in this calculation.

The reaction rate for various threshold reactions was calculated with the fluxes obtained from the DIF-2D code and the cross sections from set JM31F. Table XXIII compiles the results of these calculations. The reaction rates for iron and nickel are given per gram of the natural isotopic mixture. Although the threshold reactions are at least an order of

magnitude lower than the fission rate in  $^{235}\text{U}$  ( $\sim 8.5 \times 10^{12}$  reactions/sec/g) or in  $^{239}\text{Pu}$  ( $\sim 1.0 \times 10^{13}$  reactions/sec/g), they are sufficiently large to be observed without great difficulty.

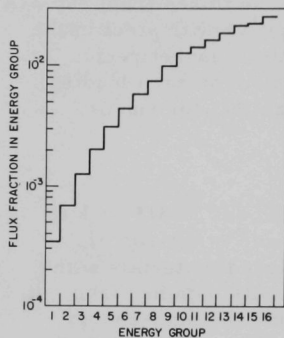


Fig. 22

Flux Spectrum above 1.35 MeV at  
Core Center in Run 31F

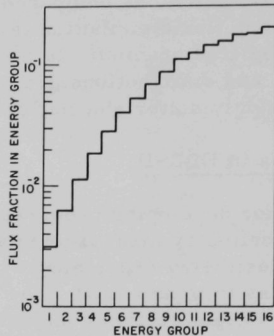


Fig. 23

Flux Spectrum above 1.35 MeV at  
Interface between Core and  
Radial Blanket in Run 31F

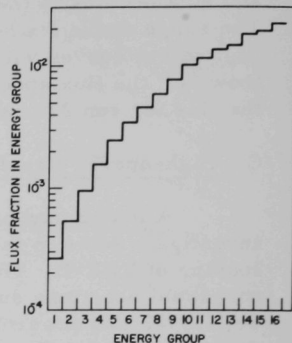


Fig. 24

Flux Spectrum above 1.35 MeV at  
Interface between Core and Upper  
Axial Reflector in Run 31F

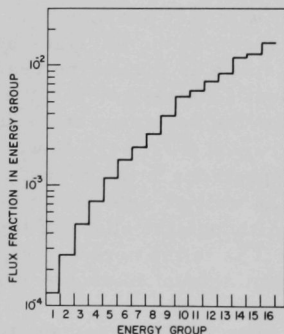


Fig. 25

Flux Spectrum above 1.35 MeV at  
~15 cm above Core in Run 31F

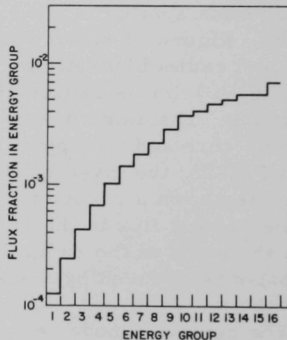


Fig. 26

Flux Spectrum above 1.35 MeV at  
~15 cm into Radial Blanket in  
Run 31F

TABLE XXIII. Rate of Various High-energy Reactions per Gram of Target Nuclide<sup>a</sup> at Three Locations in EBR-II, Run 31F

Target Element	Reaction	Rates ( $10^{10}$ reactions/g/sec)		
		Center	Radial Edge	Axial Edge
<sup>238</sup> U	n,f	51.3	25.8	30.0
<sup>238</sup> U	n,2n	1.49	0.81	0.83
<sup>235</sup> U	n,2n	1.04	0.57	0.58
<sup>239</sup> Pu	n,2n	0.22	0.12	0.12
Fe	n,p <sup>b</sup>	0.43	0.23	0.24
Ni	n,p	41.5	21.8	23.7
O <sup>c</sup>	n, $\alpha$	1.48	0.80	0.83

<sup>a</sup>Flux at core center taken as  $2.4 \times 10^{15}$  n/cm<sup>2</sup>/sec.

<sup>b</sup>Only <sup>56</sup>Fe(n,p)<sup>56</sup>Mn reaction included.

<sup>c</sup>In the form of UO<sub>2</sub>.

Two observations are made from the results in Table XXIII. First, the reaction rate for <sup>238</sup>U(n,f) is lower than that predicted by set 238. The value of the <sup>238</sup>U/<sup>235</sup>U fission ratio is also lower than that predicted by sets 238 and 23806. Second, the ratio of reaction rates at the core edge to that at core center is approximately the same for all reactions. This similarity supports the observation made earlier that the shape of the spectrum above 1.35 MeV does not change greatly in the core. For all the (n,2n) reactions, the ratio of reaction rates at the core edge is identical to that at the core center. The existence of identical ratios suggests further that the energy dependences of the three (n,2n) cross sections, which were obtained from theoretical analysis, are similar.

#### H. Comparison of the Distribution of Power by Region

The fraction of the power produced in each region of EBR-II, run 31F, was obtained from the output of the SNARG-2D and DIF-2D computer codes, and is presented in Table XXIV. The regional distribution of the power is not available from the DOT code, but the results obtained using cross-section set 23806 in the SNARG and DIF-2D calculations are in fairly close agreement. As was also true in the one-dimensional analysis, the SNARG-2D S<sub>2</sub> calculation predicts a slightly higher power in the center of EBR-II and a slightly lower power in the outer blanket than do the DIF-2D calculations. The contribution of the depleted-uranium blanket to the power production is slightly greater in the results obtained from set 238 as compared to those obtained from set 23806. This difference is attributed to the limitation

of representing the fission cross section of  $^{238}\text{U}$  by a single energy group in set 23806. The smaller fraction of the power in the inner- and outer-blanket regions, obtained from the DIF-2D code using set JM31F, is consistent with the softer spectrum produced by that cross-section set. The effect of the softer spectrum in the blanket regions is also seen in the relatively higher power produced in row 6. Better agreement between the results from sets JM31F and 238 is obtained in regions closer to the center of the core.

TABLE XXIV. Fraction of Power by Region from Two-dimensional Diffusion and Transport Calculations for Run 31F

Region Row	SNARG Code	DIF-2D Code		
	23806	23806	238	JM31F
1	0.0161	0.0158	0.0157	0.0160
2	0.0470	0.0462	0.0462	0.0469
3	0.1595	0.1565	0.1558	0.1586
4	0.1950	0.1916	0.1908	0.1941
5	0.2292	0.2285	0.2272	0.2311
6	0.2654	0.2725	0.2702	0.2753
Inner blanket	0.0656	0.0644	0.0706	0.0606
Outer blanket	0.0221	0.0246	0.0234	0.0174

#### I. Comparison of Fission-density Values

The values of the fission densities from the DOT code were normalized to 50-MWt operation of a just-critical reactor. To make the fission densities consistent with those from the MACH-1 calculations (see Section IV and Table XVIII), an energy yield per fission of 193 MeV was selected to normalize the fission densities in Tables XXV and XXVI. Table XXV lists the normalized fission densities along the vertical mid-plane for runs 27A and 31F. The values were obtained from calculations using set 23806 and an  $S_2$  transport model for both loadings in addition to an  $S_4$  transport model for run 31F. The results of the DOT and MACH 1 will be compared keeping in mind that the DOT code gives the fission density at the average radius and height in a mesh interval, rather than at the mesh points, as does the MACH-1 code.

The  $S_4$  calculation yields a flatter power-density distribution than do the  $S_2$  calculations, as was also the case for the flux. The largest percentage variation between the two calculations exists at the most distant radial position (50.03 cm), where the flux is highly anisotropic.

TABLE XXV. Radial Fission Densities from Two-dimensional Transport Calculations for Runs 27A and 31F along Core Midplane at 50 MWt

Row	Average Radius, cm	Densities, $10^{13} \text{ f/cm}^3/\text{sec}$		
		DOT $S_2$		DOT $S_4$
		Run 27A	Run 31F	Run 31F
1	0.78	3.01	2.77	2.71
	2.34	2.99	2.74	2.69
2	4.40	1.73	1.35	1.31
	6.96	1.70	1.33	1.30
3	9.58	2.54	2.30	2.27
	12.25	2.45	2.24	2.21
4	14.92	1.78	1.90	1.88
	17.61	1.77	1.79	1.78
5	20.30	1.77	1.69	1.69
	22.99	1.64	1.55	1.57
6	25.65	1.66	1.62	1.65
	28.29	1.48	1.43	1.46
7	30.97	0.0	0.200	0.198
	33.69	0.0	0.113	0.107
8	36.42	0.0	0.066	0.067
	39.14	0.0	0.038	0.044
9	42.41	0.029	0.0215	0.0278
-10	50.03	0.0081	0.0058	0.0092

TABLE XXVI. Axial Fission Densities from Two-dimensional Transport ( $S_4$ ) Calculations for Run 31F at Four Radial Positions at 50 MWt

Distance from Core Midplane, cm	Densities, $10^{13} \text{ f/cm}^3/\text{sec}$			
	Row 1	Row 6	Row 7	Row 10
-23.63	0.0	0.0	0.0248	0.00507
-21.08	0.0	0.0	0.0314	0.00570
-18.52	0.0	0.0	0.0373	0.00624
-16.01	2.07	1.13	0.0430	0.00685
-13.55	2.25	1.22	0.0487	0.00733
-11.09	2.41	1.30	0.0549	0.00786
-8.62	2.53	1.37	0.0602	0.00830
-6.16	2.63	1.42	0.0634	0.00874
-3.70	2.68	1.45	0.0658	0.00922
-1.23	2.71	1.46	0.0667	0.00924
1.23	2.70	1.46	0.0667	0.00923
3.70	2.66	1.44	0.0655	0.00920
6.16	2.59	1.40	0.0631	0.00872
8.62	2.49	1.35	0.0598	0.00829
11.09	2.35	1.28	0.0545	0.00791
13.55	2.18	1.20	0.0484	0.00738
16.01	1.98	1.11	0.0429	0.00687
18.48	0.0	0.0	0.0375	0.00625
20.94	0.0	0.0	0.0322	0.00576
23.40	0.0	0.0	0.0264	0.00517

The comparisons of the fission densities for runs 27A and 31F are limited by the substantial differences in the core loadings of these two runs. In both loadings, however, a Mark-IA driver subassembly occupies the first row, and thus the higher fission density in run 27A can be directly compared to that in run 31F. The fission density is also higher in depleted-uranium blanket subassemblies in rows 9 and 10 of run 27A as compared to that in the same blanket subassemblies of run 31F. Run 27A differs from run 31F in that no fissions occur in the run 27A inner-blanket region containing the steel reflector subassemblies; about 6% of the total fissions for run 31F occur in the depleted-uranium subassemblies in the inner-blanket region. Thus, the power and fission densities in other regions of run 27A must be higher than those for run 31F to compensate for the lack of fissions in the inner-blanket region. The higher fission densities in rows 9 and 10 of run 27A are due also in part to the greater number of fast neutrons passing through the inner-blanket region when the steel subassemblies are present.

The axial fission-density distributions at four radial positions in run 31F are given in Table XXVI from the  $S_4$  calculation. The radial positions correspond to the row 1 (0.78 cm), row 6 (25.65 cm), row 7 (33.69 cm), and row 10 (50.03 cm). The ratio of the maximum-to-minimum fission density is 1.35 in the row 1 and decreases slightly with increasing radial distance from the core center. The axial fission density reaches a maximum at slightly below the vertical midplane of the core. The asymmetry is attributed to the differences in material compositions of the regions immediately above and below the core. The region above the core contains about 48 vol % sodium, 42 vol % steel, and 10 vol % void; a mixture of 55 vol % steel and 45 vol % sodium is below the core.

#### J. Comparison of $^{235}\text{U}$ Fission Rate

Table XXVII gives the relative radial distribution of the  $^{235}\text{U}$  fission rate along the vertical midplane for five calculations of run 31F in two-dimensional geometry. For cross-section set 23806, the fission rate calculated from an  $S_4$  transport calculation lies between the values of those obtained from  $S_2$  transport calculations and diffusion-theory calculations. This comparative behavior is seen also in the power distributions and fluxes. The values obtained from cross-section set 238 are similar to those obtained from set 23806. The largest discrepancy is of the order of 2%. The relatively lower values obtained from set JM31F in the outer core and blanket regions of EBR-II can be traced to a lower  $^{238}\text{U}$  fission rate in the blanket region. As mentioned in Section H above, the inelastic cross section of  $^{238}\text{U}$  in set JM31F is greater than that in the other cross-section sets; thus, set JM31F predicts a softer spectrum and, in turn, a lower fission production in the blanket region.



TABLE XXVII. Normalized Radial  $^{235}\text{U}$  Fission Rates along Core Midplane from Diffusion and Transport Calculations of Run 31F

Row	Radial Position, cm	DOT $S_2$			DOT $S_4$		DIF-2D
		JM31F	238	23806	23806	23806	23806
1	0.78	1.0	1.0	1.0	1.0	1.0	1.0
	2.34	0.994	0.994	0.994	0.993	0.997	0.997
2	4.40	0.980	0.981	0.981	0.978	0.988	0.988
	6.96	0.962	0.965	0.965	0.963	0.973	0.973
3	9.58	0.942	0.944	0.945	0.949	0.953	0.953
	12.25	0.911	0.914	0.916	0.923	0.924	0.924
4	14.92	0.869	0.873	0.875	0.884	0.886	0.886
	17.61	0.818	0.824	0.826	0.837	0.841	0.841
5	20.30	0.762	0.768	0.770	0.786	0.790	0.790
	22.99	0.702	0.708	0.710	0.731	0.736	0.736
6	25.65	0.637	0.643	0.645	0.668	0.677	0.677
	28.29	0.567	0.574	0.575	0.598	0.614	0.614
7	30.97	0.483	0.492	0.493	0.511	0.535	0.535
	33.69	0.392	0.404	0.404	0.418	0.446	0.446
8	36.42	0.311	0.327	0.326	0.341	0.367	0.367
	39.14	0.244	0.262	0.261	0.276	0.298	0.298
9	42.41	0.181	0.200	0.198	0.213	0.228	0.228

The axial distribution of the  $^{235}\text{U}$  fission rate is given for the same five sets in Table XXVIII. All five sets exhibit the same asymmetry in the  $^{235}\text{U}$  fission-rate distribution as was seen in the fission-density distribution. The values for the locations in the core region not adjacent to the axial blanket regions are in good agreement with each other. However, in the regions above and below the core, sizable differences occur in the calculated values of the  $^{235}\text{U}$  fission rate. These differences do not have the same pattern as was seen in the radial distributions of the  $^{235}\text{U}$  fission rate. Part of the change in the pattern is due to the differences in geometry. The axial direction is similar to slab geometry; the radial direction is similar to cylindrical geometry. Another cause of the different pattern is due to the substantial change in the flux spectrum in the upper and lower reflectors. A substantial discrepancy between the results obtained from set 238 and those from set 23806 is seen for the first time in the axial  $^{235}\text{U}$  fission-rate distribution. The  $S_2$  transport calculation yields a higher value of the  $^{235}\text{U}$  fission rate than does the  $S_4$  calculation in the axial reflectors. This comparison opposes that seen in the radial distributions. The results here point out the difficulty in calculating a system that has adjoining regions of significantly different compositions (see Section III.C).



TABLE XXVIII. Normalized Axial  $^{235}\text{U}$  Fission Rates  
along Core Centerline from Diffusion and  
Transport Calculations of Run 31F

Distance from Core Midplane, cm	DOT $S_2$			DOT $S_4$ DIF-2D	
	JM31F	238	23806	23806	23806
-23.63	0.639	0.770	0.631	0.613	0.646
-21.08	0.688	0.786	0.680	0.665	0.696
-18.52	0.739	0.795	0.732	0.721	0.747
-16.01	0.795	0.810	0.787	0.782	0.798
-13.55	0.848	0.845	0.842	0.841	0.851
-11.09	0.896	0.890	0.891	0.895	0.899
-8.62	0.938	0.933	0.935	0.939	0.941
-6.16	0.972	0.969	0.970	0.972	0.972
-3.70	0.994	0.992	0.993	0.993	0.994
-1.23	1.003	1.003	1.003	1.002	1.003
1.23	1.000	1.000	1.000	1.000	1.000
3.70	0.985	0.985	0.985	0.986	0.985
6.16	0.957	0.956	0.956	0.960	0.958
8.62	0.916	0.915	0.916	0.922	0.920
11.09	0.868	0.867	0.867	0.872	0.873
13.55	0.813	0.817	0.812	0.813	0.818
16.01	0.753	0.775	0.752	0.747	0.759
18.48	0.697	0.751	0.697	0.686	0.706
20.94	0.650	0.737	0.651	0.636	0.661
23.40	0.608	0.719	0.608	0.589	0.618

#### K. Comparison of Results from One- and Two-dimensional Calculations

Some of the results from one-dimensional calculations can be compared, after the appropriate correction, to those from two-dimensional calculations. The flux,  $\bar{\varphi}$ , and the fission density,  $\rho$ , from the one-dimensional problems represent values averaged over the axial direction. The value of the flux at the core midplane can be obtained from

$$\varphi_0 = \frac{\bar{\varphi}/H_C}{\int_0^{H_C} \cos \frac{\pi}{2} \frac{z}{H_E} dz} \quad (5)$$

where

$\varphi_0$  = flux at midplane,  $\text{n/cm}^2/\text{sec}$ ;

$\bar{\varphi}$  = average flux,  $\text{n/cm}^2/\text{sec}$ ;

$H_C$  = core height, cm,

and

$H_E$  = equivalent bare core height, cm.

The spectrum and fission ratio from one-dimensional codes are also average values. Since the spectrum and the fission ratio do not change greatly in the axial direction within the core, they may be compared to the values from two-dimensional analyses without corrections. The regional power fractions from one- and two-dimensional calculations are also compared without corrections. Since the perturbation option was not available for the two-dimensional codes, no comparison is possible.

The quantities from one-dimensional diffusion calculations are given on the mesh point; the quantities from the other codes are calculated at the midpoint between the mesh points. This difference should be noted in comparing the fluxes, fission densities, etc., from one- and two-dimensional analyses.

The corrected values of the flux from one-dimensional calculations at the core center, based on 199 MeV/fission, are given in Table XXIX. The agreement of the fluxes from the one-dimensional cylindrical calculations with the DIF-2D values (Table XXI, Cases 6 and 7) is very good. The calculations in which only the core height was varied to achieve criticality give slightly better agreement than the calculations in which the reactor height was varied. The flux from the spherical representation is much lower for reasons discussed in Section IV.

TABLE XXIX. Values of the Flux at the Core Center Obtained from One-dimensional Cylindrical Calculations for Run 31F at 50 MWt

	Geometry: Cyl		Cyl	Sphere	Cyl	Cyl	Sphere
Height search	Uniform	Core	-	Uniform	Core	-	
Cross-section set	238	238	238	23806	23806	23806	
Flux, $10^{15}$ n/cm <sup>2</sup> /sec	2.570	2.496	1.945	2.581	2.509	1.943	

The fraction of the core center flux in the first 14 energy groups is given in Table XXX from one- and two-dimensional cylindrical calculations. The spectra from the two calculations made in one dimension are almost identical. The spectrum from the two-dimensional results differs only slightly from the two spectra from the 1-D analysis.

The values of the fission density along the core midplane have been given in Tables XVIII and XXV from one- and two-dimensional calculations, respectively. The results have been normalized to 50 MWt by assuming

193-MeV fission. The fission densities from the one- and two-dimensional calculations are given at slightly different locations, as explained previously.

For run 27A, the two-dimensional  $S_2$  transport and one-dimensional diffusion results are in good agreement for all radial locations. The results of one-dimensional calculations with a uniform height for the entire reactor agree more closely with the two-dimensional results than those from the 1-D calculations with different heights for core and blanket regions.

TABLE XXX. Fraction of Core Center Flux from One- and Two-dimensional Cylindrical Calculations in the First 14 Groups of Set 238 for Run 31F

Group No.	MACH 1		
	Uniform	Core	DIF-2D
1	0.0267	0.0267	0.0282
2	0.0542	0.0541	0.0535
3	0.0925	0.0926	0.0907
4	0.1267	0.1267	0.1238
5	0.1609	0.1613	0.1576
6	0.1778	0.1783	0.1729
7	0.1333	0.1335	0.1330
8	0.1020	0.1020	0.1028
9	0.0601	0.0599	0.0619
10	0.0339	0.0338	0.0367
11	0.0171	0.0170	0.0191
12	0.0094	0.0093	0.0119
13	0.0036	0.0035	0.0048
14	0.0015	0.0015	0.0021

Fission densities from  $S_2$  and  $S_4$  transport calculations and the 1-D diffusion calculation have been compared for run 31F. The  $S_4$  and diffusion results at the core center compared well; however, the  $S_2$  value is higher than the other two. Although the comparison among results for the seventh row is close, the  $S_2$  calculations yield lower fission densities than do the others in rows 9 and 10. The one-dimensional problems with different heights for core and blanket regions yield higher fission densities in row 9 and 10. With uniform reactor height, the agreement in fission densities is good between the one- and two-dimensional analyses.

The one- and two-dimensional diffusion codes give the fraction of the fissions produced by regions. Tables XIX and XXIV show that these fission values exhibit a good overall agreement for run 31F. The value from the two-dimensional calculations predicts a power fraction between the two one-dimensional calculations for row 1 of the core, but the lowest power fraction in row 6. The situation is reversed in the inner and outer blanket regions, where the values from the two-dimensional diffusion results are higher.

## REFERENCES

1. W. P. Keeney and J. K. Long, "Zero-power Reactor III (ZPR-III)," *Idaho Division Summary Report, July, August, September 1960*, pp. 45-77, ANL-6301.
2. L. J. Koch, W. B. Loewenstein, and H. O. Monson, *Addendum to Hazard Summary Report: Experimental Breeder Reactor-II (EBR-II)*, ANL-5719 (Addendum) (June 1962).
3. W. B. Loewenstein, *The Physics Design of the EBR-II*, ANL-6383 (July 1961).
4. F. S. Kirn and W. B. Loewenstein, *EBR-II Wet Critical Experiments*, ANL-6864 (Oct 1964).
5. E. Dean, Argonne National Laboratory, private communication (June 1967).
6. D. A. Meneley, L. C. Kvitek, and D. M. O'Shea, *MACH-1, A One-dimensional Diffusion-theory Package*, ANL-7223 (June 1966).
7. M. Butler, H. Greenspan, and S. Sparck, *Input Specifications for ANL Reactor Codes*, Technical Memorandum No. 93, ANL Applied Mathematics Division (Jan 1965).
8. J. T. Madell, "Multigroup Cross Section Sets for Neutronic Calculations of EBR-II," *Reactor Physics Division Annual Report, July 1, 1966 to June 30, 1967*, ANL-7310, pp. 223-228 (Jan 1968).
9. D. A. Kucera and J. T. Madell, "Analysis and Development of Neutron Cross Sections for EBR-II Studies," *Reactor Physics Annual Report, July 1, 1967 to June 30, 1968*, ANL-7410, pp. 209-213 (Jan 1969).
10. B. J. Toppel, A. L. Rago, and D. M. O'Shea, *MC<sup>2</sup>, A Code to Calculate Multigroup Cross Sections*, ANL-7318 (June 1967).
11. D. M. O'Shea, H. H. Hummel, W. B. Loewenstein, and D. Okrent, *Twenty-six Group Cross Sections*, Trans. Am. Nucl. Soc. 7, 242 (Nov 1964).
12. G. K. Leaf, A. S. Kennedy, and G. C. Jensen, *ANL-CANDID, A Two-dimensional, Diffusion-theory Code Based on CANDID2D*, ANL-7305 (Sept 1967).
13. G. J. Duffy, H. Greenspan, S. D. Sparck, J. V. Zapatka, and M. K. Butler, *SNARG-2D, A Two-dimensional, Discrete-ordinate, Transport-theory Program for the CDC-3600*, ANL-7426 (March 1968).
14. J. T. Madell, N. D. Dudey, R. R. Heinrich, and R. E. Jarka, *Analyses of Recent Dosimetry Experiments in EBR-II*, Trans. Am. Nucl. Soc. 12(2), 939-940 (1969).
15. E. M. Pennington, Argonne National Laboratory, private communication (1969).
16. F. R. Mynatt, *DOT, A Two-dimensional Discrete Ordinate Transport Code*, Report CCC 89-K-1694, Radiating Shielding Information Center, Oak Ridge National Laboratory (1968).
17. B. J. Toppel (Editor), *The Argonne Reactor Computation (ARC) System*, ANL-7332 (Nov 1967).
18. J. T. Madell, *Importance of the Weighting Spectrum in Reactivity Calculations*, Trans. Am. Nucl. Soc. 11(1), 246 (1968).

19. G. J. Duffy, H. Greenspan, S. D. Sparck, J. V. Zapatka, and M. K. Butler, *SNARG-1D, A One-dimensional, Discrete-ordinate, Transport-theory Program for the CDC-3600*, ANL-7221 (June 1966).
20. B. A. Zolotar, B. R. Sehgal, and J. M. Kallfelz, *Fast Reactor Integral Studies of Modifications to ENDF/B  $^{238}\text{U}$  Inelastic Scattering*, Trans. Am. Nucl. Soc. 12(2), 743-744 (Nov 1969).

ARGONNE NATIONAL LAB WEST



3 4444 00007957 4

